# A numerical study to investigate the roles of former hurricane Leslie, orography, and evaporative cooling in the 2018 Aude heavy precipitation event

Marc Mandement and Olivier Caumont

CNRM, Université de Toulouse, Météo-France, CNRS, Toulouse, France

**Correspondence:** Marc Mandement (marc.mandement@meteo.fr)

**Abstract.** In ~~southeastern~~ south-eastern France, the Mediterranean coast is regularly affected by heavy precipitation events. On 14–15 October 2018, in the Aude department, a back-building quasi-stationary mesoscale convective system produced up to about 300 mm of rain in 11 h. ~~The synoptic situation was perturbed by the former hurricane Leslie ,~~ At synoptic scale, the former hurricane Leslie was involved in the formation of a Mediterranean surface low that ~~focused the convective activity~~channelled conditionally unstable air towards the coast. At mesoscale, convective cells focused west of a ~~quasi-stationary cold front~~decaying cold front, that became quasi-stationary, and downwind of the terrain. To investigate the roles of the moisture provided by Leslie, orography and evaporative cooling ~~in the processes that led to the~~ among the physical processes that led to the location and intensity of the observed rainfall, numerical simulations are run ~~and evaluated with~~ at 1 km and 500 m horizontal resolutions and evaluated with independent near-surface analyses ~~comprising standard and~~ including novel crowd-sourced observations of personal weather stations. Simulations show that, in a first part of the event, low-level conditionally unstable air parcels found inside strong ~~updrafts mainly originate from the Mediterranean Sea, east of 4.5 E,~~ updraughts mainly originated from areas east of the Balearic Islands, over the Mediterranean Sea, whereas in a second part, an increasing number ~~originates~~ originated from Leslie's remnants. Air masses from ~~east of 4.5 E appear~~ areas east of the Balearic Islands appeared as the first supplier of moisture over the entire event. Still, Leslie contributed to substantially moisten mid-levels over the Aude department, diminishing evaporation processes. Thus, the evaporative cooling over the Aude department ~~does~~ did not play any substantial role in the stationarity of the ~~cold~~ quasi-stationary front. Regarding lifting mechanisms, ~~most of the air parcels found inside strong updrafts~~ the advection of conditionally unstable air by a low-level jet towards the quasi-stationary front, confined to altitudes below 2 km, reactivated convection along and downwind of the front. Most of the air parcels found inside strong updraughts near the location of the maximum rainfall ~~are lifted above the cold front, attesting its key role in focusing convection~~were lifted above the quasi-stationary front. Downwind of the Albera Massif, mountains bordering the Mediterranean Sea, cells formed by orographic lifting ~~seem to be~~ were maintained by low-level leeward convergence, mountain lee waves and a favourable directional wind shear; when terrain is flattened, rainfall is substantially reduced. The location of the exceptional precipitation ~~appears to be driven primarily~~ was primarily driven by the location of the quasi-stationary ~~cold~~ front and secondarily by the location of convective bands downwind of ~~the~~ orography.

## 1 Introduction

Heavy precipitation events (HPEs), usually defined as events with daily rainfall exceeding 150 mm (Ricard et al., 2012), affect all the coastal areas of the western Mediterranean region, often producing flash floods (Nuissier et al., 2008). Due to the large societal impact of these events causing casualties and damage, they were extensively studied during the HyMeX programme extending from 2010 to 2020 ~~(Drobinski et al., 2014; Ducrocq et al., 2014)~~(Ducrocq et al., 2016). Large rainfall amounts observed in time periods from few hours to several days during HPEs are the result of ~~convective activity~~ deep convection focusing over the same area. ~~Strong convective activity~~ Convective organization often consists in continuous convective cell renewal constituting quasi-stationary mesoscale convective systems (MCSs). ~~The total rainfall amount observed over a given area is the product of both rainfall intensity produced by individual cells and the time period during which this convective activity remains focused over this area.~~

Ricard et al. (2012) built a climatology of HPE environments over the ~~northwestern Mediterranean area . Synoptic situations favouring these~~ north-western Mediterranean area based on 3D-Var ALADIN mesoscale analyses of a 5 yr period (2002–2006). With this climatology, synoptic situations favouring HPEs over Languedoc-Roussillon, maritime part of the Occitanie region in southern France (Fig. 1), are now well known. At upper levels, a trough extends over the Iberian peninsula in a ~~southeast-northwest~~ south-east–north-west orientation. This trough is associated with a cold low in the middle and high troposphere and generally entails a diffluent ~~southwesterly~~ south-westerly flow at upper levels. MCSs develop preferentially northwards of a slow-evolving surface low located between ~~Spain~~ the Iberian Peninsula and the Balearic Islands focusing a ~~southeasterly~~ south-easterly low-level jet (LLJ). The location and the deepening of the slow-evolving surface low ~~has been identified as a key ingredient in focusing the convective activity~~ is a key ingredient in focusing convection over the same area and continuously initiating ~~convective activity~~ convection inside MCSs (Duffourg et al., 2016; Nuissier et al., 2016). The Mediterranean Sea supplies moisture – up to 60 % of the total air parcels moisture in previous HPEs according to water budgets of Duffourg and Ducrocq (2013) – and heat to this low-level airflow through evaporation and heat exchange, which both depend on the sea surface temperature (SST). ~~Lebeaupin et al. (2006) showed that~~ Thus, abnormally warm SST can destabilize atmospheric lower levels up to ~~2000–3000~~2–3 ~~m.In some HPEs, the Mediterranean Sea supplied up to 60 % of the total air parcels moisture (Duffourg and Ducrocq, 2013; Duffourg et al., 2018),~~ km above sea level (a.s.l.) (Lebeaupin et al., 2006), modulating the intensity of convective precipitation. All these ingredients favour a persistent LLJ transporting low-level conditionally unstable air parcels over the Gulf of Lion.

Several mechanisms are responsible for lifting ~~the~~ this conditionally unstable low-level marine flow~~when it reaches the coast~~, triggering convection over the same area. First, the mountainous terrain bordering the Mediterranean shore leads to orographic lifting. Secondly, in the lower levels of the atmosphere, ~~low-level~~ mesoscale boundaries, when stationary, can lift air parcels over the same areas. ~~These mesoscale boundaries are found in fronts~~ Such stationary boundaries can be fronts (Trapero et al., 2013), outflow boundaries of cold pools, local convergence lines, mesoscale pressure troughs, among others. Lifting mechanisms include mechanical lifting in convergence areas and ~~density departures between air massesthat cause the most buoyant air parcels to ascend.~~

The orography-like lifting buoyancy differences between air masses. The action of these mesoscale boundaries is combined with the action of the terrain itself (Ducrocq et al., 2008; Duffourg et al., 2018). This and explains why large rainfall amounts are observed over the mountains as well as in the Mediterranean plains and over the sea . These mesoscale boundaries can pre-exist, or being initiatedby the first convective cells. The idealized study of Bresson et al. (2012) shows that the occurrence of these mesoscale boundaries is dependent on the characteristics of the upstream flow: for example cold pools have been shown to form preferentially when the flow is relatively dry or weak. Once initiated, the location and intensity of these features (Duffourg et al., 2018). Once convection initiated, the locations of these mesoscale boundaries and the amplitudes of their temperature, humidity, pressure and wind speed gradients can be continuously modified by the MCS thanks to small-scale feedback mechanisms of the convection to the environment (Duffourg et al., 2016). Cold pools, which are favoured by a dry or weak upstream low-level flow according to the idealized study of Bresson et al. (2012) over southern France, are affected by such feedback mechanisms. In previous HPEs, dry air parcels at altitudes between 1 and 4 km a.s.l., when mixed to precipitation of the MCS, were humidified and cooled through evaporation processes, forming vigorous downdraughts resulting in the formation or maintenance of cold pools (Ducrocq et al., 2008; Duffourg et al., 2018).

During the Among these mechanisms, those at the origin of the HPE of the night of 14 to 15 October 2018, in the center and northwest on which this article focuses, are studied. During that night, in the centre and north-west of the Aude department (Fig. 1), part of Languedoc-Roussillon, rainfall accumulations over 200 mm in less than 12 h affected an approximately 60 km long and 10 km wide band oriented southeast to northwestsouth-east to north-west. Inside the band, an automatic rain gauge in Trèbes (Fig. 2) measured 295.5 mm in 11 h including 243.5 mm in 6 h and 110.5 mm in 2 h. Météo-France volunteer observers measured 318.9 mm in Conques-sur-Orbiel and 306.6 mm in Cuxac-Cabardès with manual rain gauges in 2 days, probably fallen almost entirely in 12 h as 93 to 99 % of the 2-day rainfall fell in 12 h in nearby Météo-France automatic rain gauges. In the center and northwestern centre and north-western part of the band, such 12 h rainfall accumulations were unprecedented in recent meteorological records and return periods were estimated over 100 yr. The orientation of the band, parallel to the small Trapel river catchment, led to a major flash flood in this catchment in particular, overflowing and destroying bridges. It caused 15 fatalities, 75 injured and around 325 millions euros of damages including € 256 M to insurable assets for around 29 000 insurance claims and € 69 M to non-insurable assets (Préfecture de l'Aude, 2018; Ayphassorho et al., 2019; French Insurance Federation, 2019; Petrucci et al., 2020). This episode is part of a series of HPEs that occurred in October and November 2018 over the north-western Mediterranean and particularly affected the Balearic Islands on 9 October (Lorenzo-Lacruz et al., 2019) and Italy on 27–30 October (Davolio et al., 2020).

As described by Caumont et al. (2020) and Kreitz et al. (2020) Kreitz et al. (2020) and Caumont et al. (2021), at large scale, a remarkable and unusual feature of this event is the landfall of the former hurricane Leslie feature was the extratropical transition of hurricane Leslie before landfall in the Portuguese coast on the evening of 13 October, one day before the Aude HPE started. It is still unknown how the additional moisture provided by Leslie contributed HPE started. Transitioning hurricanes over the North Atlantic are known to disturb the midlatitude flow close or downstream of them, causing or modifying the location and intensity of high-impact weather such as HPEs (Grams and Blumer, 2015; Pantillon et al., 2015). As hurricanes can supply large amounts of moisture and because the moisture structure in the lower troposphere was shown to play a key

role in the timing and location of precipitation of previous HPEs (Lee et al., 2018), it is of interest to quantify the amount of moisture supplied by Leslie to the convective system. At a smaller scale, largest rainfall accumulations ~~are found to be~~ were aligned along bands downstream of the Pyrenees relief. Within the bands, the largest accumulations ~~are~~ were found west of a quasi-stationary ~~cold~~ front and a quasi-stationary mesoscale trough. Because of the heavy ~~rain observed in the area, evaporative cooling processes may have played a role in the stationarity of the cold front.~~ convective rain observed west of this front, evaporative cooling may have additionally cooled the west side of the front. This additional cold air may have caused a dynamic feedback that contributed to the stationarity of the front. Similar dynamic feedback was described by Davolio et al. (2016) over north-eastern Italy: in cases of upstream events, a cold-air layer formation preceded the convection onset and evaporation and sublimation of precipitation beneath the convective system were able to additionally cool this cold-air layer, which influenced the propagation of this cold-air mass. Consequently, the goal of the article is to address the ~~questions raised by Caumont et al. (2020): what was (i) the origin of moisture including Leslie's contribution, (ii) the role of the~~ following questions raised by Caumont et al. (2021): what were the roles of (i) the moisture provided by Leslie, (ii) the eastern Pyrenees relief and (iii) the ~~role of the~~ evaporative cooling in the physical processes that ~~supplied conditionally unstable air, triggered convection and led to the observed rainfall?~~

led to the location and intensity of the observed rainfall? Investigation of these questions is carried out as follows. First, the case study is presented in Sect. 2. Numerical simulations of this HPE ~~produced with the Meso-NH model~~ are described in Sect. 3. The realism of the reference simulation is evaluated in particular near the surface through a comparison with independent analyses built from screen-level observations of standard and personal weather stations (Mandement and Caumont, 2020) in Sect. 4. ~~Once evaluated, the simulation chosen as reference~~ The reference simulation and a simulation to study the sensitivity to the terrain are used in Sect. 5 to investigate processes that led to the observed rainfall, in particular the role of Leslie. Then, the role of the cooling associated with the evaporation of precipitation is evaluated in Sect. 6.

## 2 Case description

~~The synoptic situation over Europe between~~

### 2.1 Synoptic-scale situation

Between 13 and 15 October, the synoptic situation over western Europe was disturbed by the remnants of ~~two Atlantic hurricanes , Leslie and Michael , and their associated fronts (NOAA NESDIS, 2018).~~

hurricanes Leslie and Michael (NOAA NESDIS, 2018), while the situation remained blocked over eastern Europe due to a quasi-stationary high at all levels of the troposphere. At 500 hPa, on 13 October 12:00 UTC, a large trough extended from the west of Iceland towards the west of Portugal (Fig. 3b). ~~On~~ The trough split and evolved in a cut-off low over Spain on 14 October 12:00 UTC (Fig. 3d), ~~part of the trough split and evolved in a cut-off low over Spain, while the remnants of~~ while the remnants of former hurricane Michael generated a secondary trough at the rear of the cut-off. On 15 October 12:00 UTC (Fig. 3f), this secondary trough ~~joined~~ merged with the existing cut-off low ~~. The interaction between both lows, merged into a~~

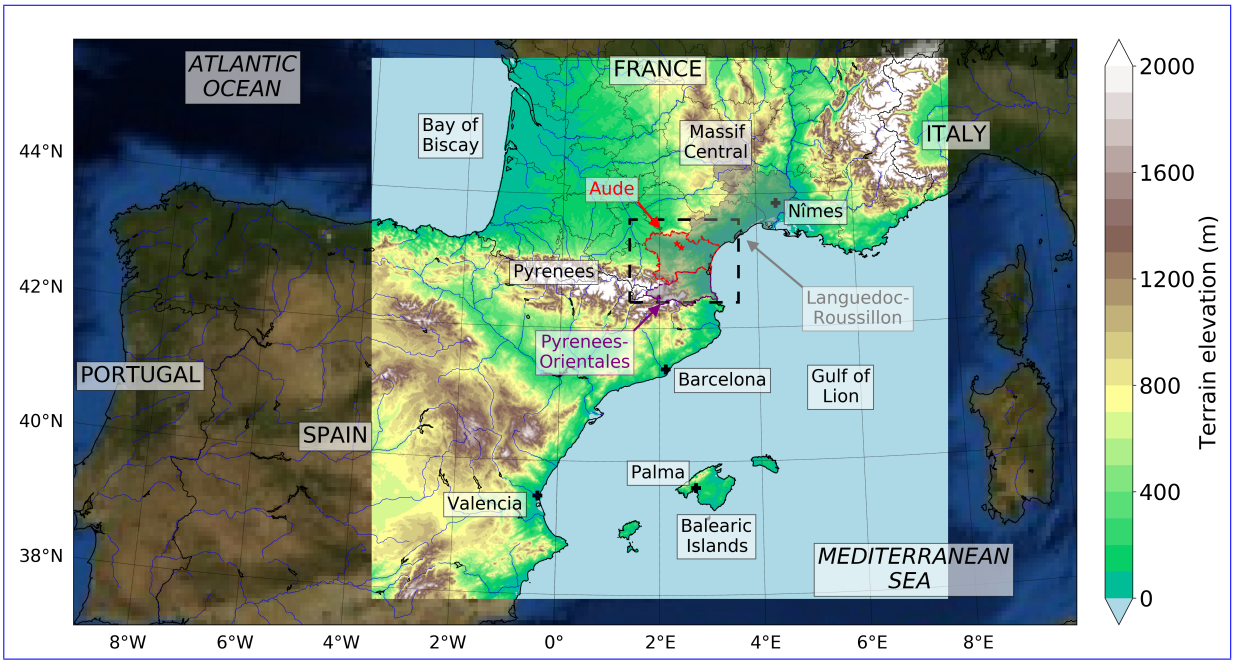


**Figure 1.** Map of ~~southwestern~~ south-western Europe~~where locations mentioned in the article are indicated~~. The bright square and the dashed black line correspond to the two grid-nested model domains~~(parent and child) of the simulation~~. Inside the bright square, terrain elevation from the parent model is shown; outside, it is the NASA visible blue marble image (from https://visibleearth.nasa.gov). Solid black lines indicate French departments and country borders. Languedoc-Roussillon, a region including Aude and ~~Pyrénées-Orientales~~ Pyrenees-Orientales departments is shaded. The two little red stars, landmarks displayed in other figures, indicate from north to south the ~~location~~ locations of Villegailhenc and Trèbes, which are two towns ~~strongly~~ that were affected by the HPE.

~~single cut-off low, seems to have strongly slowed the westward movement of this mid-level cut-off low. Also, the cut-off low was prevented from moving westwards by the blocked situation observed over eastern Europe between 13 October 12:00 UTC and 15 October 12:00 UTC, due to a quasi-stationary high at all levels of the troposphere.~~ which slowed its eastward movement.

~~Between 14 October 12:00 UTC and 15 October 12:00 UTC, a small jet branch circumvented to the south the cut-off low. This jet branch reached maximum values over the Aude department of around 30 m s$^{-1}$ at 300 hPa and around 25 m s$^{-1}$ at 500 hPa. During this period, this jet showed some diffluence over the Aude department and changes were observed in its speed and direction due to the movementof the cut-off low. From southerly, the jet backed southeasterly, temporarily veered southwesterly at 300 hPa and then slowed down.~~

Near the surface, on 13 October 12:00 UTC (Fig. 3a), category 1 hurricane Leslie approached the Portuguese coast ~~. A cold front along a mean sea level pressure (MSLP) trough linked Leslie to a low located over Ireland. At 15:00 UTC, few hours before reaching the coast, Leslie was a category 1 hurricane with a 979 hPa estimated central MSLP (NOAA NWS National Hurricane Cent~~ ~~. Leslie was declared post-tropical cyclone at 21:00 UTC, just before landfall over Portugal between 21:00 and 22:00 UTC~~

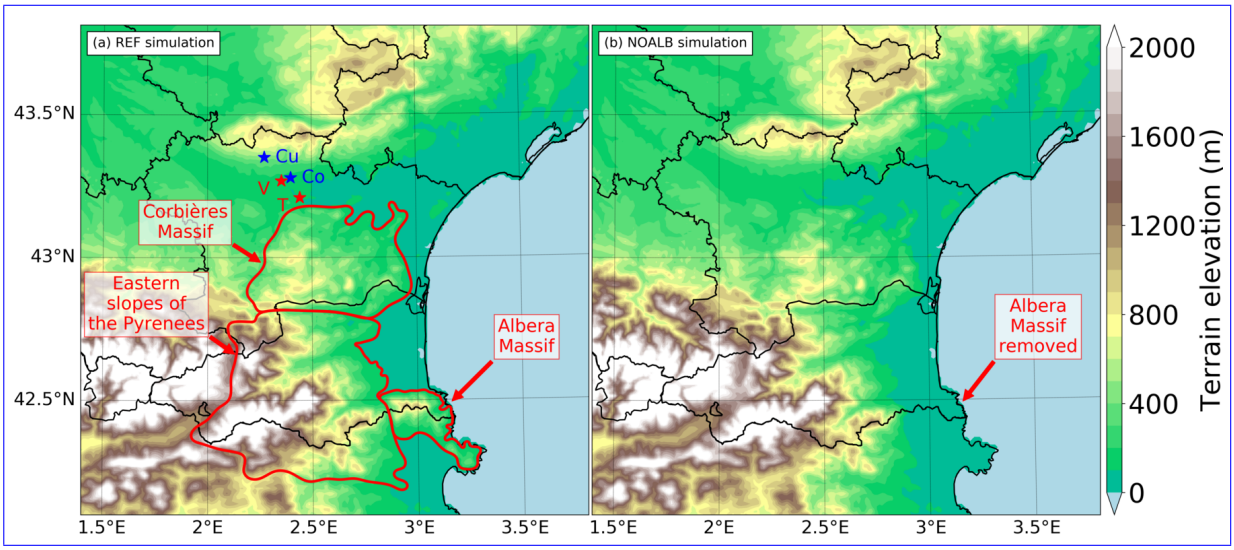


**Figure 2.** Orography of the south Languedoc-Roussillon including the Aude department in the simulations (a) REF and (b) NOALB in which the Albera Massif is removed. Solid black lines indicate French departments and country borders. Stars indicate towns which were affected by the HPE~~and mentioned in the article~~: "V" is Villegailhenc, "T" is Trèbes, "Cu" is Cuxac-Cabardès and "Co" is Conques-sur-Orbiel. ~~The two red stars are landmarks displayed in other figures of the article.~~ Red contours indicate mountain massifs.

~~(NOAA NWS National Hurricane Center, 2018b). Leslie~~ (NOAA NWS National Hurricane Center, 2018a). Leslie brought a large amount of moisture at all levels of the troposphere: over large areas, water vapour mixing ratio exceeded 12 g kg$^{-1}$ at 925 hPa (Fig. 4a), 7 g kg$^{-1}$ at 700 hPa (not shown) and 2.5 g kg$^{-1}$ at 500 hPa ~~just before Leslie's landfall according to ARPEGE analyses .~~ (not shown) according to ARPEGE analyses on 13 October 18:00 UTC. These values are in the upper range of mixing ratios observed within the boundary layer over the Gulf of Lion by Di Girolamo et al. (2016) (8–15 g kg$^{-1}$) or within the free troposphere below 3 km above ground level (2–8 g kg$^{-1}$) over the Balearic Islands by Chazette et al. (2016) during southerly marine flows of the HyMeX SOP1. Leslie made landfall in Portugal between 21:00 and 22:00 UTC (NOAA NWS National Hurricane Cente as a post-tropical cyclone. After landfall, Leslie's MSLP low filled up quickly, and ~~remnants of this former hurricane participated to extend towards south the existing cold front. On~~ Leslie's remnants participated to extend towards south and increase the activity over Spain and France of the existing cold front on 14 October ~~12:00 UTC~~ (Fig. 3c)~~, the cold front has become more active over Spain and France~~. During the evening and the night of 14 to 15 October, around the cold front, in an area of deep convection, a low rapidly deepened over the Mediterranean Sea, between the Balearic Islands and Valencia region ~~around this cold front, associated with strong convective activity.A potential vorticity anomaly at upper levels is observed upstream of this~~ (Fig. 3e). A trough formed and extended this Mediterranean low towards Languedoc-Roussillon (Caumont et al., 2021). This low ~~. It may have helped to deepen it through a baroclinic interaction, but its precise role would need further investigation.~~

~~This Mediterranean low moved slowly northwards overnight . It~~ moved slowly northwards overnight which increased the MSLP gradient along the Languedoc-Roussillon coast~~and more generally over the Mediterranean Sea. Consequently, the~~

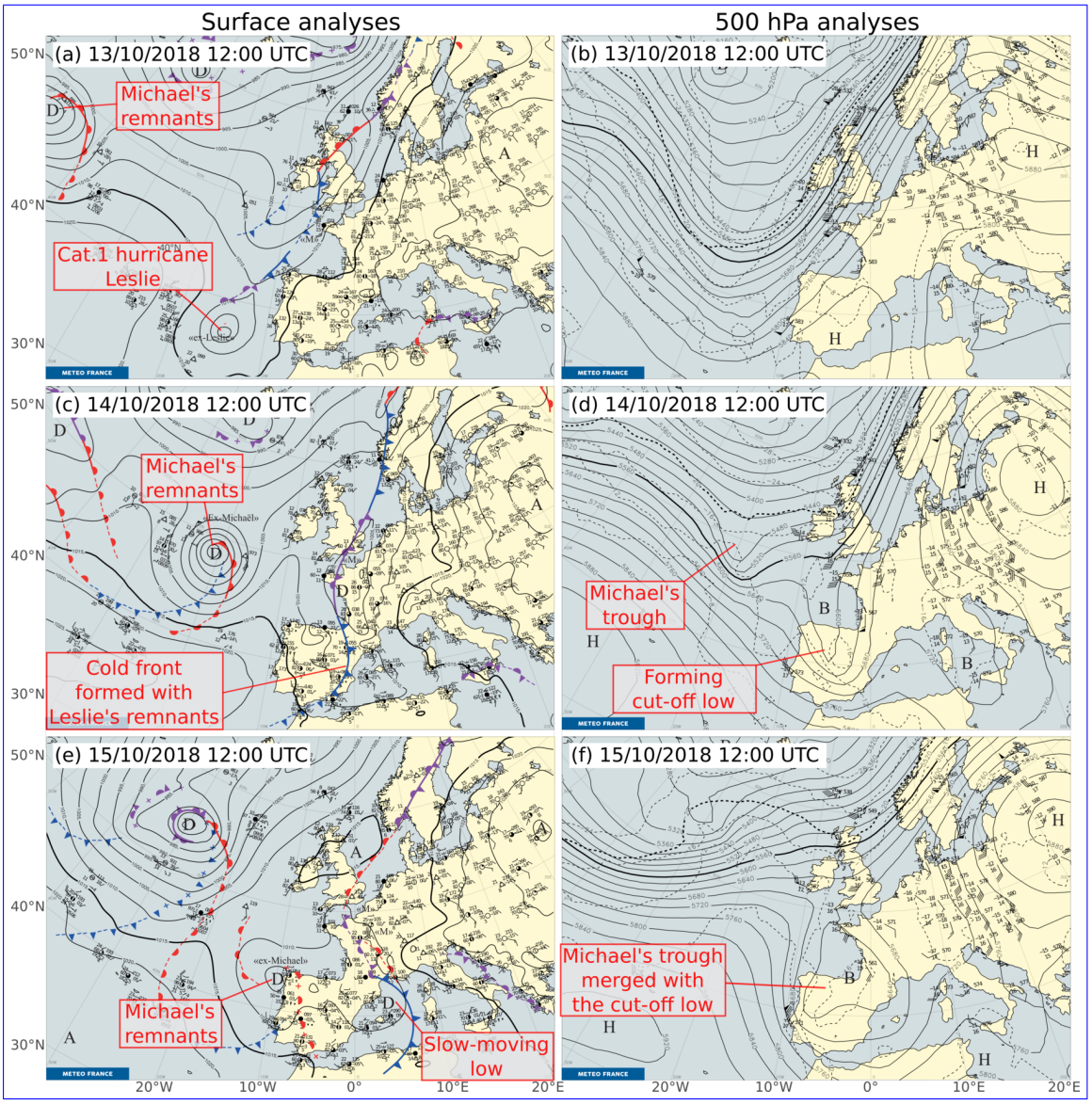


**Figure 3.** Météo-France (a,c,e) ~~Surface~~ surface and (b,d,f) 500 hPa analyses ~~of Météo-France national forecast department~~ (Santurette and Joly, 2002) at (a,b) 12:00 UTC 13 October 2018, (c,d) 12:00 UTC 14 October 2018 and (e,f) 12:00 UTC 15 October 2018. Surface fronts are manually ~~drawned~~ drawn using conventional observations, satellite, radar images and short-term forecasts (instead of analyses due to availability time constraints). Mean sea level pressure (in hPa), 500 hPa geopotential height (in gpm) and temperature (in °C) are from ~~Météo-France~~ the operational global model ARPEGE (Courtier et al., 1991) 6 h forecast of the T – 6 h run (T: time of the chart). Surface (respectively altitude) low-pressure centres are indicated by "D" (resp. "B") and high-pressure centres by "A" (resp. "H").

~~near-surface east-southeasterly wind strengthened, increasing LLJ supply in warm and moist air originating~~ . Consequently, the

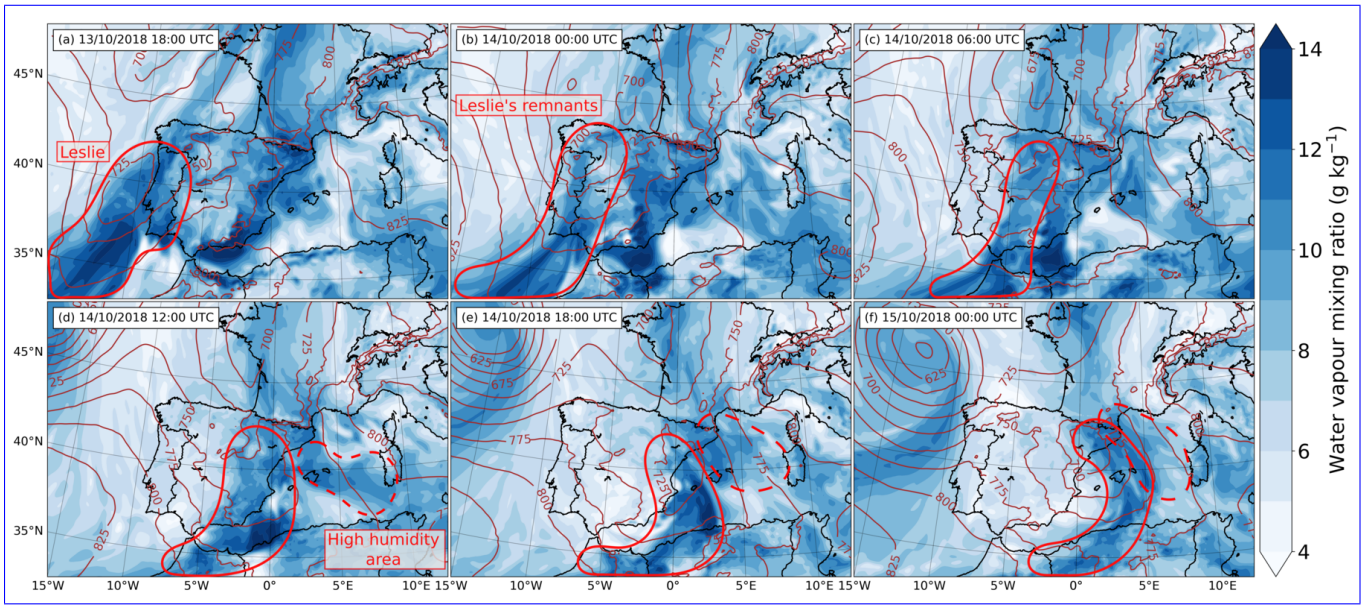


**Figure 4.** ARPEGE analyses of water vapour mixing ratio and geopotential height (in gpm) at 925 hPa on 13 October 2018 at (a) 18:00 UTC, on 14 October 2018 at (b) 00:00 UTC, (c) 06:00 UTC, (d) 12:00 UTC, (e) 18:00 UTC, and (f) on 15 October 2018 at 00:00 UTC. The approximate location of moist air masses carried by Leslie (solid red line) or found over the Mediterranean Sea (dashed red line) are circled.

east–south-easterly wind between the surface and 925 hPa strengthened (not shown). This resulting LLJ supplied significantly moist air from the Mediterranean Sea (dashed lines in Figs. 4d-f).

~~Caumont et al. (2020) show that a trough formed and extended this low towards Languedoc-Roussillon. At the same time,~~ ~~part of the active cold front (~~In the meantime, on 14 October, the active part of the cold front located north of the Pyrenees (called CF1~~) producing thunderstorms north of the Pyrenees (~~, Fig. 3c) moved ~~westwards. Its precipitating activity decreased as it moved west, but its thermal signature near the surface remained .~~ eastwards. CF1 decayed (precipitation along it decreased and almost stopped) as it moved east (not shown), while its near-surface mark in the form of a thermal gradient remained (Caumont et al., 2021). Then CF1 stopped in the middle of the Aude department and became a quasi-stationary front, slightly west of the MSLP trough. Both CF1 and the MSLP trough remained quasi-stationary between 22:30 UTC 14 October and 04:00 UTC 15 October (Caumont et al., 2021).

~~The advance northeastwards~~ In the morning of 15 October, the north-eastwards advance of the slow-moving low and its associated cold front (CF2, Figs. 3c,e) brought additional low-level moisture over Languedoc-Roussillon. ~~At low-levels, this moisture originates from both from~~ This moisture originated from both Leslie's remnants and a moist area ~~already present over Spain (solid lines in~~ over southern Spain (Fig. 4). ~~Kreitz et al. (2020) indicate that these different moisture contributions resulted in values of precipitable water up to 35 mm during the HPE. CF2 left the Aude department in the morning of the 15 October, which ended the HPE over the department.~~

~~A focus on the mesoscalesituation shows that rain started over the Pyrénées-Orientales~~

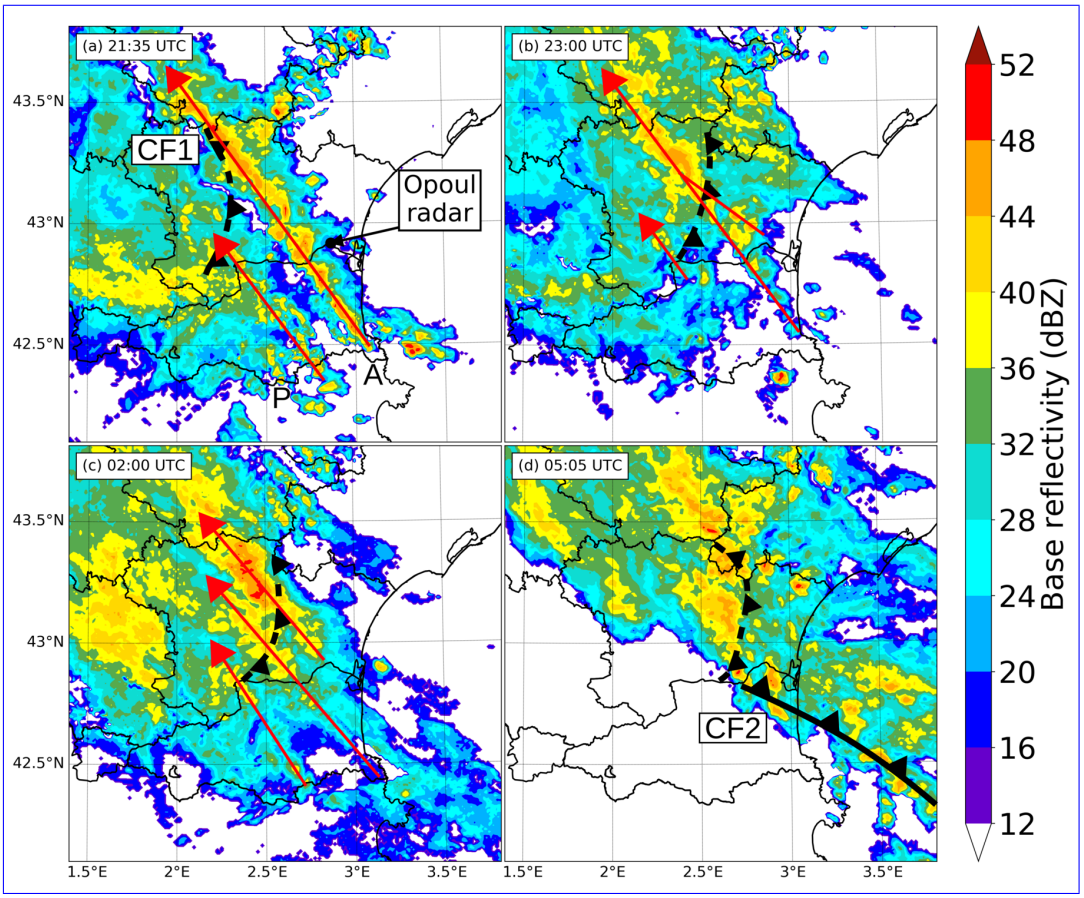


**Figure 5.** Radar base reflectivity from ~~the French~~ Météo-France operational mosaic on 14 October at (a) 21:35 UTC, (b) 23:00 UTC and on 15 October at (c) 02:00 UTC and (d) 05:05 UTC. Red arrows ~~with triangle arrowheads~~ show the axes of continuous convective cell renewal and the movement of individual cells shown by radar. ~~Dashed lines~~ "A" and ~~large red arrowheads indicate~~ "P" recall the ~~northeastwards movement~~ location of the ~~convective system ahead~~ Albera Massif and the eastern slopes of the Pyrenees, respectively. Locations of CF1 and CF2 are indicated by bold black frontal symbols.

## 2.2 Mesoscale situation

At mesoscale, rain started over the Pyrenees-Orientales and Aude departments in the morning of 14 October. ~~Météo-France standard weather stations in Pyrénées-Orientales recorded 0 to 20 mm rainfall, even 50 mm locally near the Spanish border, rainfall amounts being higher over mountains, between 02:00 and~~ A first part of the HPE began around 19:00 UTC 14 October~~. In Aude, 0 to 11 mm rainfall was recorded between 13: 00 and 19~~: ~~00~~east of a large area of stratiform rain advected from Spain, two parallel lines of convective cells formed (red arrows in Fig. 5a), starting over the Albera Massif and the eastern slopes of the Pyrenees, and rapidly became the active parts of a back-building MCS. The eastern line was more active than the western line: reflectivities exceeded 40 ~~UTC. Observed rainfall was a share between convective cells locally formed and either~~

convective cells or stratiform rain crossing the Pyrenees mountains from Spain. Clouds advected from Spainoriginated from a large cloud band ahead of CF2.

Over the Aude and Pyrénées-Orientales departments, the most intense rainfall occurred between 19: 00dBZ at 21:35 UTC 14 October and 07:00along the eastern line but remained below 40 UTC 15 October (Fig. 5dBZ along the western line (Fig. 5a). One shall note that the Opoul radar marked in Fig. 5a(Fig. 5a), well covering the area, had a failure between 21:55 UTC 14 October and 06:05 UTC 15 October. The three closest radars that filled the gaps are located to the northwest, north and northeast, outside of the area shown in Fig. 5. Thus, : observed reflectivities are likely underestimated in Figs. 5b-d particularly around and south of the Opoul south of this radar.

The first part of the HPE begins around 19:00 UTC 14 October. At that time, the size of the stratiform area and rainfall intensity increased due to an increasing rain advection from Spain. East of this rainy area, near the Mediterranean coast, two parallel lines of convective cells formed, starting over the Albera Massif and the eastern slopes of the Pyrenees, and rapidly became the active parts of a back-building MCS. Fig. 5a exhibits these two parallel lines along the red arrows. The eastern line was more active than the western line: reflectivities exceed 40 dBZ at 21:35 UTC along the eastern line but remain below along the western line. At At 23:00 UTC, Fig. 5b shows convective cores feeding this that convective cores fed the eastern line from its eastern flank with reflectivities particularly strengthened in the northwestern part of the lineand that reflectivities were particularly strengthened in the north-western part of the line, west of CF1. This organization in two lines is was observed until around 00:00 UTC. After 00:00 UTC, the eastern line orientation slightly turned anticlockwise and a third active line formed , visible in Fig. 5c. Enhanced reflectivities along this line seems to originate in the eastern (Fig. 5c) starting from the upstream slopes of the Corbières Massif. Reflectivities of all lines are still strengthened in their northwestern were still strengthened in their north-western parts. At 02:00 UTC , more reflectivities are observed over the Mediterranean Sea, south of the red dashed line in Fig. 5c, showing the advance of the convective system ahead of (Fig. 5c), an extended region of reflectivity > 12 dBZ appeared over the Mediterranean Sea showing the advance of the rain band associated with CF2. The large red arrows and the dashed lines in Figs. 5c,d indicate the movement and the northeastern limit of this rain band , respectively. After 02:00 UTC, in the a second part of the HPE, this rain band associated with CF2 modified the MCS organization in lines observed until then: active cells with reflectivity above 40 dBZ were continuously advected from the sea. Heavy rainfall persisted in the areaover the Aude department, strengthened in particular west of the red dash-dotted line shown in Fig. 5dthat corresponds to the location of CF1 (Fig. 5d). After 05:00 UTC, the large rain band associated with CF2 headed slowly northeastwards, leaving no more precipitation behindnorth-eastwards and precipitation stopped around 07:00 UTC over the western part of the Aude department (around 09:00 UTC over the entire department, not shown).

Fig. 6a shows the resulting 24 h accumulated precipitation from the ANTILOPE analyses, the Météo-France operational algorithm of quantitative precipitation estimation at a Standard and Personal Weather Stations (SPWS) ANTILOPE quantitative precipitation estimate (QPE) at 1 km horizontal resolution , blending radar and rain gauge observations (Champeaux et al., 2009) . In this case, available rain gauge observations from personal weather stations have been added to the product after a manual quality control, and validated by Caumont et al. (2020) over independent rain gauges. In ANTILOPE analyses, maximum accumulated precipitation reaches blending radar and SPWS rain gauge observations, described by Caumont et al. (2021).

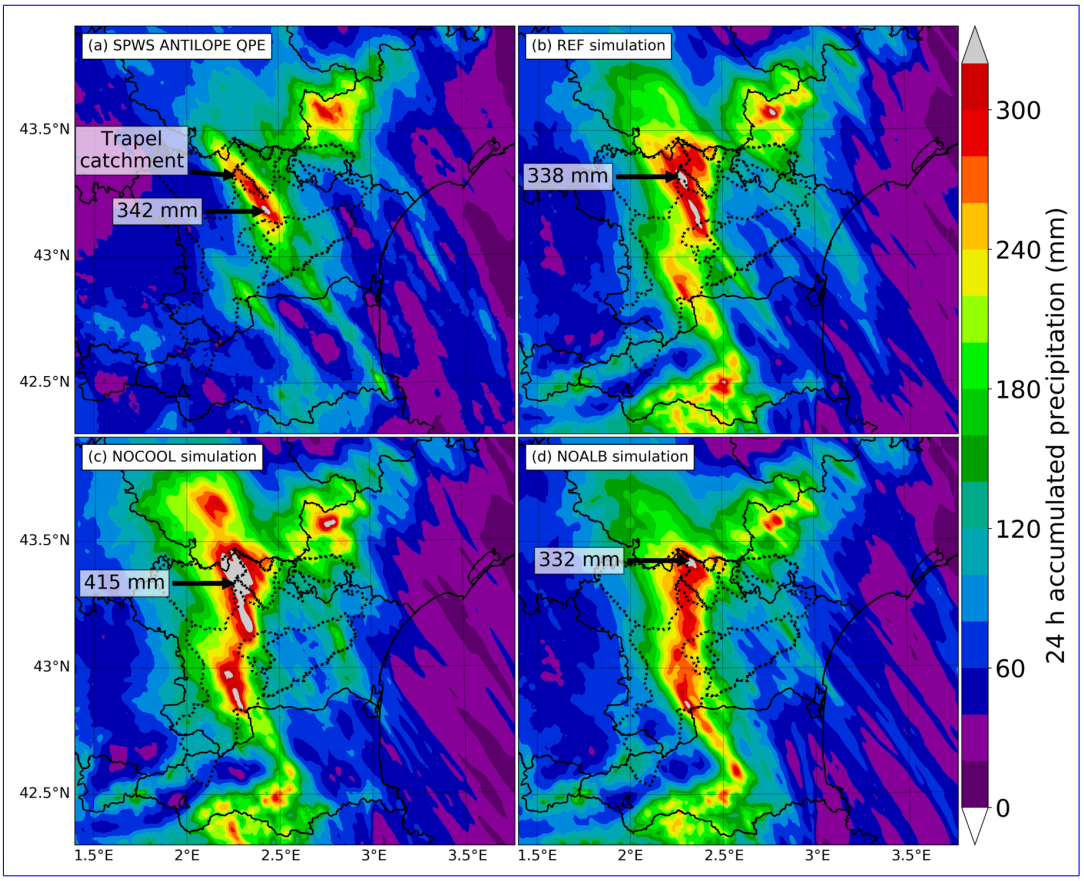


**Figure 6.** 24 h accumulated precipitation between 12:00 UTC 14 October and 12:00 UTC 15 October from the (a) SPWS ANTILOPE ~~analyses~~QPE, (b) REF, (c) NOCOOL and (d) NOALB simulations. Solid black lines indicate French departments and country borders. Dotted black lines indicate catchment limits of the Aude basin and its tributaries.

Estimated accumulated precipitation reached 342 mm few kilometres ~~southwest~~ south-west of Trèbes, where an automatic rain gauge measured 295.5 mm and close to a personal weather station that measured 311 mm. The line organization identified on radar observations resulted in two precipitation bands, referred to as eastern and western bands, with the eastern band a little curved, due to the formation of the aforementioned third line between 00:00 and 02:00 UTC. The consequences were catastrophic near the ~~observed~~ precipitation maximum, because most of the rain ~~has fallen~~ fell in 6 to 12 h. Another local maximum of ~~precipitation of~~ 317 mm ~~is observed over mountains, northeast of the bands . Consequences in this mountainous area were low since it is accustomed to such rainfall and~~ was estimated over mountains, north-east of the bands but without reported consequences since hourly precipitation accumulations remained moderate.

## 3 Numerical simulations

Simulations are performed with the ~~French~~ non-hydrostatic numerical research model Meso-NH version 5.4.2 (Lac et al., 2018), extensively used to study Mediterranean MCSs (Bouin et al., 2017; Martinet et al., 2017; Duffourg et al., 2018).

### 3.1 Meso-NH configuration

A two-way interactive grid nesting is chosen in order to study the sensitivity to a modification of model physics only within the child ~~'s model domain. A parent domain with a~~ domain. A 960 × 900 km$^2$ horizontal domain ~~over southern France and northwestern Mediterranean Sea is defined (Fig. 1). To realistically represent precipitating systems, a model configuration close to that of the French convection-permitting operational model AROME (Seity et al., 2011; Brousseau et al., 2016) is chosen with a~~ at 1 ~~km horizontal resolution for the parent domain . The child's model horizontal domain is centered over the Aude department with~~ km resolution covering southern France and the north-western Mediterranean Sea is chosen for the parent domain and a 180 × 135 km$^2$ ~~domain and a~~ horizontal domain at 500 m ~~horizontal resolution .~~ resolution centred over Aude is chosen for the child domain (Fig. 1). For both domains, configurations close to the AROME operational model (Seity et al., 2011; Brousseau et al., 2016) are chosen to realistically simulate deep convection. The Gal-Chen and Somerville (1975) height-based vertical coordinate is used with 89 stretched vertical levels from 5 m up to 23.75 km~~(height of the mass point)~~, including 33 levels below 2 km height. ~~The number and spacing of vertical levels is designed to be similar to AROME. A Rayleigh damping is progressively applied above 15 km height (i.e. the last 7 levels) to the perturbations of the wind components and the thermodynamical variables with respect to their large-scale values in order to prevent spurious reflections from the upper boundary. It has a maximum value at the top of the upper absorbing layer of 0.001 s$^{-1}$.~~

~~For the momentum transport scheme, a fourth-order centered discretization is used (CEN4H), while the transport scheme used for meteorological (temperature, water substances and turbulent kinetic energy) and scalar variables is a monotonic version of the piecewise parabolic method (PPM_01). The time integration scheme chosen is a fourth-order explicit Runge-Kutta (RKC4) and the model time step is 2 s for the parent, 1 s for the child. To suppress very short wavelength modes, a fourth-order diffusion operator is applied to the wind components (u,v,w) with an e-folding time (time at which waves are damped by a factor $e^{-1}$) of 1800 s.~~ Simulations start on 14 October at 12:00 UTC and last 24 h~~. The~~ , with initial and lateral boundary conditions of the parent model ~~are given by AROME operational~~ given by AROME analyses every 3 h~~at 1.3 km horizontal resolution. The lateral boundary conditions of the AROME analyses are provided by the latest available operational ARPEGE short cut-off analyses and forecasts (4 ARPEGE runs per day). For example, the analysis and 3-h forecast of the 06:00 UTC ARPEGE run provide lateral boundary conditions for 06:00 and 09:00 UTC AROME analyses. There is one particular case for AROME 00:00 UTC analysis that receives its lateral boundary conditions from a very short cut-off ARPEGE 00:00 UTC analysis.~~. Further details are given in Appendix A.

~~Earth surface variables and fluxes are simulated with the SURFEX model version 8.1 (Masson et al., 2013). Each grid mesh is divided in four main tiles. The following schemes are used for each tile: a three layer force-restore version of ISBA for natural land surface (Noilhan and Planton, 1989), TEB for urban area (Masson, 2000), the roughness length formula of~~

Charnock (1955) with Louis (1979) exchange coefficients for lake and the COARE 3.0 parametrization (Fairall et al., 2003) for sea-surface fluxes. COARE 3.0 is used as recommended by Rainaud et al. (2016) for Mediterranean HPEs and used by Lebeaupin Brossier et al. (2009) and Bouin et al. (2017). Optional corrections of sea-surface fluxes due to density effects during heat and water vapour transfer (Webb et al., 1980) and precipitation effects (Gosnell et al., 1995; Fairall et al., 1996) are applied. The SST field comes from the initial AROME analysis and remains constant for the entire simulation. Physiographic files used include the land cover data base ECOCLIMAP-II/Europe version 2.5 (Faroux et al., 2013), SRTM topography with a horizontal grid spacing of approximately 250 m (Farr et al., 2007) and soil properties derived from harmonized world soil database (HWSD; FAO, IIASA, ISRIC, ISS-CAS, JRC (2012)).

Regarding physical parametrizations, the longwave radiation scheme used is the Rapid Radiation Transfer Model (Mlawer et al., 1997) while the shortwave scheme is based on Fouquart and Bonnel (1980) method. Full radiation computations are performed once every 15 min. For turbulence, the one dimensional parametrization used is based on a 1.5-order closure (Cuxart et al., 2000) of the turbulent kinetic energy equation with the Bougeault and Lacarrere (1989) mixing length. At 1 km resolution, deep convection is assumed to be resolved explicitly by the model's dynamics. Shallow convection is parametrized with the Pergaud et al. (2009) Eddy Diffusivity Mass Flux scheme. The bulk one-moment mixed microphysical scheme used is ICE3 (Pinty and Jabouille, 1998; Caniaux that includes six water species (water vapour, cloud droplets, raindrops, pristine ice crystals, snow or aggregates and graupel).

For the child model at 500 m horizontal resolution, in the so-called turbulence "grey zone", the choice of a 1D turbulence parametrization can be questioned. This choice was made to keep consistency between the two coupled models. Investigations of Machado and Chaboureau (2015) showed that 1D turbulence parametrization produces too many small cloud systems and rain cells with a shorter lifespan than observed. Although very sensitive to the in-cloud mixing length chosen, 3D turbulence parametrization appears more consistent with observations. Further investigations, out of the scope of the study, are required on Mediterranean cases to compare 1D and 3D turbulence parametrizations at 500 m resolution. Preliminary investigations were done by Martinet et al. (2017) showing some improvements by using a 3D turbulence parametrization with 3 different mixing lengths in simulations of a Mediterranean HPE at 500 m horizontal resolution compared to a 2.5 km resolution simulation using a 1D turbulence parametrization. Because of the difference in horizontal resolution, it is difficult to conclude what benefit came from the highest resolution or from the turbulence scheme.

Regarding computation setup, each experiment was computed on the Météo-France supercomputer Bullx DLC b710 "Beaufix" with 3200 cores (40 cores by node for 80 nodes) in approximately 14 h. The Meso-NH model was compiled at an optimization level 2 (O2) in order to produce bit reproducible results.

### 3.2 Experiments

Three simulations are shown in the study. The first one is run to realistically simulate the case. Validation of its realism is performed in Sect. 4. This reference study is carried out to realistically simulate the rainfall observed during the case and is called REF hereafter.

The importance of mountains bordering the Mediterranean shore in focusing or enhancing convection was pointed out by Ducrocq et al. (2008) in the 1999 Aude HPE that affected an area 30 km east of the one affected in the 2018 Aude HPE. The

authors hypothesized that the Massif Central and the Pyrenees probably enhanced the intensity of the rainfall by channelling the warm and moist LLJ. Removing the Massif Central diminished the maximum precipitation simulated though it had not a substantial impact on the stationarity of the simulated MCS, organized along a narrow line (Nuissier et al., 2008). However the removal of Pyrenees mountains, located upstream of the precipitation maximum, was not tested.

In the 2018 Aude HPE, radar observations in Figs. 5a-c show that a large number of convective cells were continuously initiated during several hours over the Albera Massif and remained aligned downstreamsecond simulation, called NOALB, investigates the role of the Albera Massif on precipitation. The Albera Massif is the easternmost Massif of the Pyrenees bordering the Mediterranean Sea (Fig. 2); its highest mountain is the Neulos peak which culminates at an altitude of 1256 m. Its altitude is 1023 m (respectively 1128 m) in the father parent (resp. child) model. In the 2018 Aude HPE, radar observations in Figs. 5a-c show that a large number of convective cells were continuously initiated during several hours over the Albera Massif and remained aligned downstream. These observations support the occurrence of quasi-stationary convective bandingthat can lead to large rainfall accumulations. Similar convective band generation was observed in the southeastern south-eastern flank of the Massif Central by Miniscloux et al. (2001) and Cosma et al. (2002)upstream of : rainfall bands were enhanced on the lee side of small-scale topography ridges, with an enhancement of these bands on the lee side of the topography ridges. Cosma et al. (2002) showed in both idealized and real-case simulations that the extension of precipitation lines downwind of orography resulted (i) from from (i) the formation of a mountain wave immediately downwind of the crest and (ii) from the lee-side convergence created by deflection around the obstacle. Sensitivity tests indicated that the structure (length, width) and the intensity of the rain band are were quite dependent on the upwind meteorological conditions and on the topographic configuration. The strengthening of convection downstream of small-scale topographic structures due to lee-side convergence was also noted by Ricard (2005) during the 1995 Cévennes HPE. Barrett et al. (2015) attributed a similar event over the UK to lee-side convergence combined with thermally forced convergence resulting from elevated heating over the upstream terrain.

Thus, to clarify the effect of the Albera Massif on precipitation, a simulation replacing it by a flat terrain, called NOALB, is carried out. Inside the Albera Massif area bounded by the red solid line , or Barrett et al. (2015) over the United Kingdom, combined in that last case with thermally forced convergence. Also, the Albera Massif could have played a role on precipitation in previous HPEs such as the 1999 Aude HPE described by Nuissier et al. (2008) and Ducrocq et al. (2008). In 1999, precipitation remained stationary along a narrow line and the precipitation maximum was found 30 km east of the 2018 Aude HPE maximum, downstream of the Albera Massif which was identified as one of the source of lifting (see parcel number 1 in Fig. 9 of Ducrocq et al., 2008) . In NOALB, the Albera Massif (Fig. 2a) terrain elevations above , red solid lines) is flattened at a constant altitude of 25 m a .s.l. are set to 25 m a.s.l., except west of the area in order to avoid the massif in order to avoid an abrupt transition to higher terrain. From the western limit of the areaWest of the Albera Massif, terrain elevations are set to gradually decrease at a rate of 40 m every km eastwards (4 % slope) until reaching 25 m a.s.l. Such transition is not necessary north or south of the Albera Massif because terrain elevation is mainly below 25 m. a.s.l. The topography resulting from these changes is shown in Fig. 2b.

In previous HPEs such as the 2002 Gard case or the HyMeX IOP13 case, evaporation processes have been shown to play an important role in cooling the air near the ground (Ducrocq et al., 2008; Duffourg et al., 2018). In these previous cases, dry air parcels at altitudes between 1000 m and 4000 m, when mixed to precipitation, were humidified and cooled through evaporation

processes, forming vigourous downdraughts resulting in the formation and maintenance of cold pools. In the 2018 Aude HPE, the role of evaporative cooling in modifying the location The third simulation, called NOCOOL, investigates the role of the evaporation of raindrops in cooling the cold sector west of CF1 , changing the duration and its influence on the movement of CF1stationarity or substantially cooling the cold sector west . Indeed, because convective cells are formed or enhanced downstream of CF1 is questioned.To clarify the effect of the cooling associated with the evaporation of precipitation on the case study, this process is switched off (Fig. 5), enhanced evaporative cooling could serve to anchor CF1 at the same location since downdraughts of these cells do not destroy the frontal zone (Chappell, 1986). In NOCOOL, negative temperature tendency from evaporation of raindrops is set to zero for the child model (black dashed square in Fig. 1)but kept for the parent model (bright square in Fig. 1) in a simulation called NOCOOL. Because of the two-way setup chosen, changes applied to the child model interact with the parent model. This change is applied only to the child model because applying these modifications to the entire parent model strongly modifies MSLP and wind fields upstream of Languedoc-Roussillon, probably because cooling processes have a strong influence on the life cycle of the low over the Mediterranean Sea (not shown) . Applying these modifications only to the inner domain allows us to quantify the impact of this process only over the south of Languedoc-Roussillon where strongest precipitation is observed. , which allows us to quantify the impact of this process only over the area affected by the HPE.

## 4 Validation of the REF simulation near the ground

## 4 Validation of the REF simulation

Since the initial conditions of REF are provided by the AROME analyses in which all conventional observations are assimilated, there is little deviation from these observations at the initial time. At 12:00 UTC 14 October, comparison of REF fields on all vertical levels to high resolution soundings of Nîmes, Barcelona and Palma (not shown, see Fig. 1 for the locations) reveal absolute bias (respectively root mean square error) of $< 0.3$ K (resp. $< 0.6$ K) in temperature, $< 0.3\,\mathrm{g\,kg^{-1}}$ (resp. $< 0.8\,\mathrm{g\,kg^{-1}}$) in water vapour mixing ratio, $< 0.5\,\mathrm{m\,s^{-1}}$ (resp. $< 1.9\,\mathrm{m\,s^{-1}}$) in wind speed and $< 7°$ (resp. $< 16°$) in wind direction.

Because the stationarity of precipitation is correlated to the quasi-stationarity of a MSLP trough and a virtual potential temperature ($\theta_v$) gradient (Sect. 2.1), and because of the availability of near-surface observations that are not assimilated in the AROME model, this section focuses on validating the REF simulation near the surface. Near-surface fields of the REF simulation are compared to independent gridded SPWS analyses built from screen-level observations of standard and personal weather stations, called SPWS analyses, SPWS described by Mandement and Caumont (2020). Instead of directly comparing the two fields, to separate disentangle physical departures from departures due to gridding methodsboth gridding methods and model features that cannot be resolved by the observation network used in the SPWS analyses, REF is interpolated in the same way as the SPWS analyses. This interpolationis called REF_SP. The method , called REF_SP, consists in replacing the value and altitude of each weather station used in the SPWS analyses by the value and altitude of REF nearest grid point. Then, with , keeping the exact same weights and gridding methodused in the SPWS analyses, the REF_SP gridded field is built. The method gives information about model features that are not resolved by the observation network used in the SPWS analyses. . Thus, in

this section, the REF_SP ~~interpolations~~ fields are compared to the SPWS analyses (the REF fields are also shown to illustrate the method). For precipitation~~fields~~, REF is directly compared to the ~~ANTILOPE analyses because they are on regular grid whose resolution is close to that of the model~~SPWS ANTILOPE QPE since the horizontal resolution of radar observations used in the QPE is close to the horizontal resolution of REF.

Regarding rainfall accumulations, the REF simulation is able to reproduce the organization ~~of precipitation in two bands oriented southeast to northwest~~ in two bands oriented south-east to north-west (Figs. 6a,b) ~~and located approximately as the observations. Local maxima of both bandsare also~~ found in the QPE. Both bands, including local maxima, are located quite correctly. Along the eastern band, two local precipitation maxima are simulated: a first one north of the Trapel catchment with 338 mm and another one with 331 mm at the same latitude but 7.3 km west of the ~~observed~~ 342 mm QPE maximum. Rainfall along the southern part of this eastern band is underestimated. Along the western band, the local maximum is largely overestimated with 296 mm whereas the ~~observation~~ QPE estimates 206 mm and in the southern part of the band, simulated rainfall amounts reach more than twice the observations. In the upper right corner of Fig. 6b, the shape of the area affected by heavy rainfall and the maximum accumulated rainfall simulated (343 mm) are similar to ~~observations~~ QPE (317 mm ~~observed~~estimated). Elsewhere, the REF simulation generally overestimates rainfall, particularly over orography. These overestimations are substantial north and east of the local maximum indicated by the black arrow (Fig. 6b) or over the Pyrenees mountains.

Regarding the timing of rainfall ~~, the first part of the HPE begins around 19:00 UTC 14 October both in REF and in observations (see Sect. 2). Until 23:00 UTC, rainfall simulated is less intense than observed particularly along the eastern band: north of it, hourly rainfall above 20 mm is observed after 21:00 UTC but simulated only after 23:00 UTC. The REF simulation is able to reproduce the convective lines that are observed mostly in the first part of the HPE but substantial rain rates along these lines are simulated later than in observations. The second part of the event begins~~ (not shown), REF simulates longer rain than observed over the Aude department, particularly over its western part. The HPE begins at the same time as in observations, but the beginning of the second part (around 05:00 UTC in ~~the REFsimulation whereas it is 02:00 UTC in observations. Finally, the HPE ended when the rain band associated with the cold front CF2 left the Aude department. It left the~~ REF) as well as the end of rainfall over the western part of the Aude department (~~respectively the entire Aude department) heading northeastwards~~ around 10:00 UTC ~~(resp.~~ in REF) are delayed by 3 h; this delay reduces to 1.5 h regarding the end of rainfall over the entire Aude department (around 10:30 ~~UTC) in the REFsimulation, while it was observed around 07:00 UTC (resp. 09:00 UTC). So, it rained longer over the Aude department in the REFsimulation than in observations, particularly in the western part of the department~~UTC in REF).

~~As described in Sect. 2, Caumont et al. (2020) show that the location of a MSLP troughand a virtual potential temperature ($\theta_V$) gradient remained quasi-stationary between 22:30 UTC 14 October and 04:00 UTC 15 October. The ability of REF to accurately model these two features is evaluated.~~

~~Regarding MSLP~~Regarding the location of the MSLP trough, at 00:00 UTC, ~~both the SPWS analysis (Fig. 7a) and~~ REF_SP (Fig. 7b) ~~show the MSLP trough. REF_SP locates the trough slightly west compared to the analysis. MSLP is up to 3 hPa higher in the northern part of the trough in analyses compared to REF_SP. At 06:00 UTC, analysis (Fig. 7d)shows that the MSLP~~

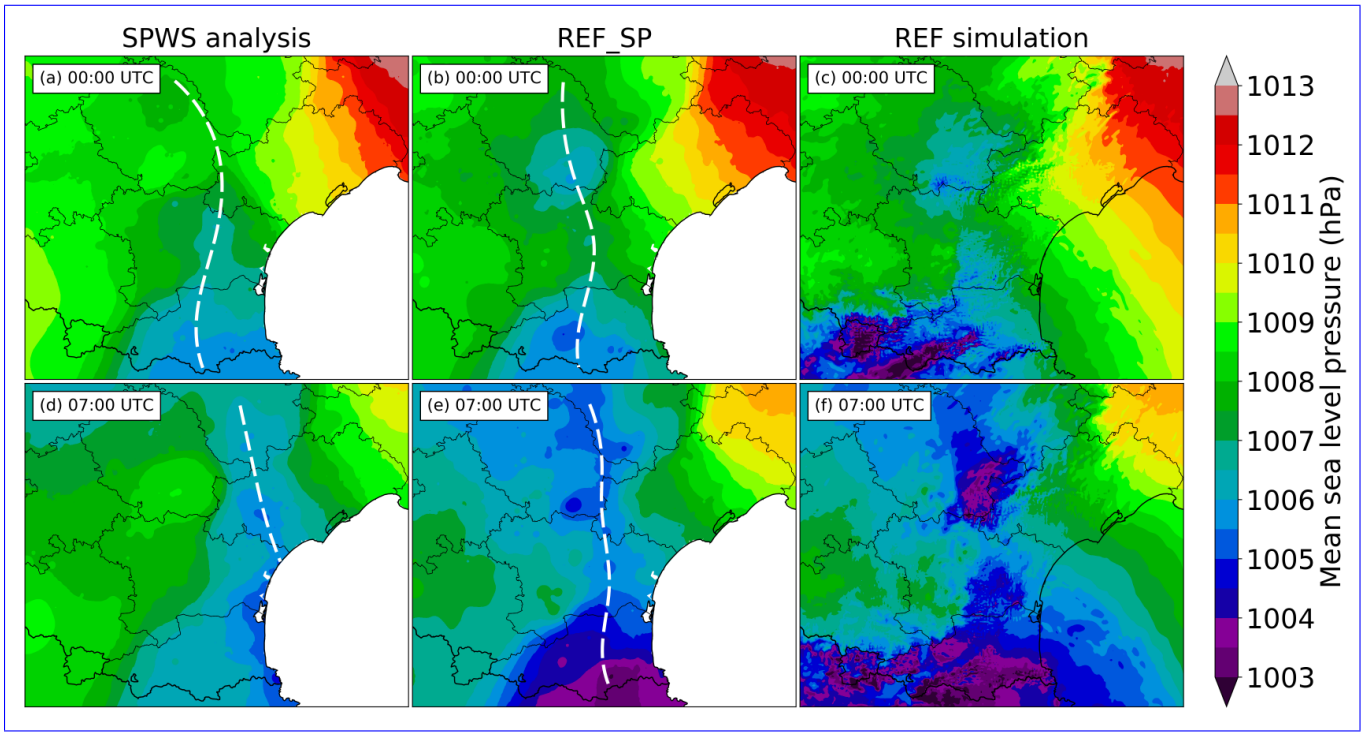


**Figure 7.** Mean sea level pressure on 15 October at (a,b,c) 00:00 UTC and (d,e,f) ~~06~~07:00 UTC from (a,d) the SPWS analysis, (b,e) REF_SP and (c,f) the REF simulation. Solid black lines indicate French departments and country borders. Dashed white lines indicate the approximate location of the MSLP trough. Analyses are not computed over the Mediterranean Sea, in white, because of the lack of ~~surface~~ near-surface observations over sea.

~~trough moved 30 km eastwards whereas the REF simulation (Fig. 7e) shows that the trough barely moved since 00:00 UTC. In both cases, the trough deepened between 00:00 UTC and 06:00 UTC. REF_SP keeps the trough at a~~ locates it slightly west compared to the SPWS analysis (Fig. 7a). Then, the trough remains quasi-stationary ~~location~~ in REF_SP until about 07:00 UTC ~~whereas analyses indicate the trough remained quasi-stationary only until about 04:00 UTC, before moving eastwards.The comparison between REF_SP and the SPWS analysis~~ (Fig. 7e), which reveals a time lag of approximately 3 h in the movement of the trough ~~in the morning of 15 October~~compared to the SPWS analysis.

~~Regarding $\theta_V$ at screen level, at 23:00 UTC, SPWS analysis (Fig. **??**a) locates in the middle of the Aude department the $\theta_V$ gradient which is a salient feature of the cold front CF1. In the analysis, $\theta_V$ is below 18 °C west of CF1 and above 20 °C east of it. REF_SP (Fig. **??**b) shows a similar amplitude of $\theta_V$ gradient at the approximate same location as the SPWS analysis but $\theta_V$ is 1 °C higher on both sides of CF1. This shows that the location of CF1 given by REF simulation (Fig. **??**c), slightly more west of what is seen in Figs. **??**a,b, is consistent with the SPWS analysis. The sharp east-west $\theta_V$ gradient is also consistent with the observations even if REF overestimates by approximately 1 °C the virtual potential temperature on both sides of CF1. In fact, the comparison between Figs. **??**a ,b,c shows that the surface observation density is unable to seize the precise location~~

~~Location of the 19 °C virtual potential temperature ($\theta_v$) isotherm at 2 m height between 19:00 UTC 14 October and 09:00 UTC 15 October from (a) the SPWS analysis, (b) REF_SP and (c) the REF simulation. Terrain elevation over 750 m above sea level (a.s.l.) is shaded in grey. Red stars show the location of Villegailhenc (northern star) and Trèbes (southern star), towns strongly damaged by the HPE.~~

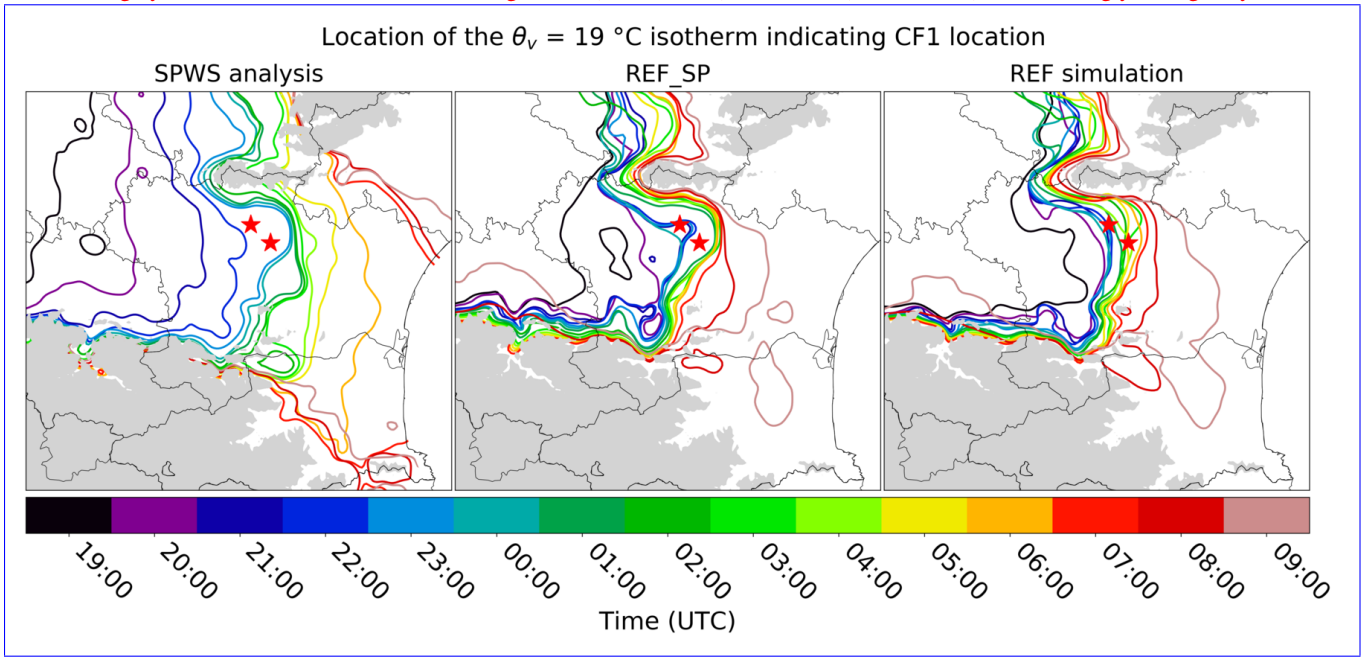


**Figure 8.** Location of the 19 °C virtual potential temperature ($\theta_v$) isotherm at 2 m height between 19:00 UTC 14 October and 09:00 UTC 15 October from (a) the SPWS analysis, (b) REF_SP and (c) the REF simulation. Terrain elevations above 750 m a.s.l. are shaded in grey. Red stars are as in Figs. 1,2.

~~of $\theta_v$ gradient such as the one given by REF. At 04:00 UTC, $\theta_v$ decreased by as much as 2 °C west of CF1 in the SPWS analysis(Fig. **??**d) and decreased by less than 1 °C in REF_SP (Fig. **??**e) compared to the state at 23:00 UTC. This decrease is essentially due to a temperature decrease, relative humidity remaining between 90 and 100 % at 23:00 and 04:00 UTC. In the SPWS analysis, south of the Aude department, CF1 moved eastwards: such displacement is not observed in REF simulation (Figs. **??**e,f).~~

~~To finely describe the movement of~~ Regarding the movement of CF1~~, the location of the~~ , whose location is indicated by the 19 °C $\theta_v$ ~~isotherm is shown in Fig. 8. SPWS analysis (Fig. 8a) shows that CF1 moved eastwards between 19~~isotherm, REF_SP simulates a quasi-stationarity that begins around 21:00~~and 22:00 UTC. It remained quasi-stationary east of the two red stars between~~ UTC (22:30 UTC in the SPWS analysis) and ~~04~~ends around 07:00 ~~UTC. After that time,it moved eastwards and reached the Mediterranean Sea around 06~~UTC (04:~~30 UTC. REF_SP (Fig. 8b) shows that CF1 became quasi-stationary earlier, around 21~~:00 ~~UTC, and remained quasi-stationary until 07:00 UTC. It reached the Mediterranean Sea around 09:30 UTC.~~ UTC in the SPWS analysis) according to Figs. 8a,b. Thus, CF1 is quasi-stationary approximately 4.5 h longer in REF than in analyses~~and reaches the Mediterranean Sea with a 3 h delay in REF compared to analyses.~~ .

Regarding the location where CF1 remained quasi-stationary, setting aside delays, REF_SP generally locates CF1 slightly ~~more~~ further west than the SPWS analyses, but the westwards shift remains mostly below 10 km. Comparison between REF_SP and REF (Figs. 8b,c) shows some small-scale movements of CF1 simulated by REF that cannot be reproduced in REF_SP~~. It gives insight about~~ , indicating the magnitude of departures that cannot be seized by the SPWS analyses and thus should not be considered as substantial.

~~Fig. ?? shows~~ This small westward shift is confirmed by the comparison of 10 m height ~~horizontal wind simulated by REF with surface observations superimposed. At~~ REF wind fields with near-surface observations (not shown), comparison which also reveals that inland, between CF1 and the coast, REF slightly underestimates the wind speed and simulates south-eastern instead of eastern wind directions in some places.

Regarding $\theta_v$ gradient amplitude (not shown), at 23:00 UTC, REF~~simulates 12 to 16~~ _SP simulates a similar amplitude as the SPWS analyses even if $\theta_v$ is 1 ~~m s$^{-1}$ southeasterly to east-southeasterly winds blowing over the Mediterranean Sea near the Languedoc-Roussillon shore. Inland, east of~~ °C higher in REF_SP than in analyses on both sides of CF1~~, east-southeasterly winds reach mostly 6 to 12 m s$^{-1}$. West of CF1, westerly 0 to 6 m s$^{-1}$ winds are observed. These opposite winds cause strong wind convergence at CF1 location. Small differences are identified between REF and observations around CF1: they support that CF1 location is 0 to 10 km further west in the REFsimulation than in the SPWS analyses . Inland, between CF1 and the coast, observations support eastern wind direction more than southeastern direction and indicate slight underestimations. At~~ . Between 23:00 and 04:00 UTC, ~~as a result of the approaching Mediterranean low, REF wind speed increased east of~~ west of CF1, ~~reaching 14 to 18~~$\theta_v$ is simulated to decrease by less than 1 ~~m s$^{-1}$ over the Mediterranean Sea and 8 to 14~~°C while analyses indicate a decrease of 2 ~~m s$^{-1}$ inland. At that time, 3 stations indicate westerly winds while REF indicates the opposite, showing that REF simulates CF1 location 10 to 15 km further west than observed~~°C, which show little differences between simulation and observations.

In summary, the REF simulation produces realistic near-surface fields in comparison with the SPWS analyses and scattered wind observations. The main differences ~~between analyses and REF~~ are substantial time lags in the stationarity of mesoscale boundaries: the MSLP trough and CF1 ~~remained~~ remains quasi-stationary between 3 to 4.5 h longer over the Aude department in the REF simulation than in the SPWS analyses. After 04:00 UTC, it results in an approximately 3 h delay in the movement of these mesoscale boundaries in REF compared to analyses. This longer stationary period probably ~~caused the~~ causes prolonged rainfall over the area that may explain some of the overestimations found. Also, the westerly shift of about 10 km found between REF and the SPWS analyses in the quasi-stationary location of CF1 or the MSLP trough is correlated with the similar westerly shift found in the location of the heaviest precipitation between REF and the ~~ANTILOPE analysis. The amplitude of both shifts is about 10 km.~~ SPWS ANTILOPE QPE. Keeping in mind these departures, the REF simulation is ~~considered realistic enough to study the case and is~~ taken as the reference in the following sections.

## 5 Origin of the conditionally unstable air and lifting mechanisms

This section investigates what mechanisms ~~supplied~~ supply conditionally unstable air to the convective system, including studying whether its moisture comes from areas that ~~have been~~ are particularly humidified by Leslie's remnants. Trajectories and thermodynamic properties of air parcels that ~~contributed~~ contribute to the formation of the strongest convective cells in the REF simulation as well as those of cold parcels located west of CF1 are described. Lifting mechanisms are also studied, in particular the role of the Albera Massif. To carry out the investigation, a series of backward trajectories are computed using the Lagrangian trajectory tool of Gheusi and Stein (2002). ~~Atmospheric~~ It is based on the technique of Schär and Wernli (1993) in which three Eulerian passive tracers are initialised with the initial grid point position and are advected online by the resolved and subgrid-scale wind; a review of existing Lagrangian trajectory tools is given by Miltenberger et al. (2013). The starting point of the backward trajectories are atmospheric columns with strong mid-level ~~updrafts~~ updraughts close to the location of the 24 h maximum rainfall~~are selected~~. Inside each column, 40 air parcels taken every 2 vertical levels of the model from the second level (18 m height) to the 80$^{th}$ (~~13~~about 13.5 ~~568 m~~ km height) are followed and their trajectories are shown in the figures. Some trajectories (in grey in Fig. 9a) are not projected on ~~the vertical sections~~ vertical sections either when vertical movements of the air parcels are of small amplitude around the Aude department~~;~~ , or when a trajectory intersects the terrain along the projection axis because the terrain along the axis differs substantially from the one along the trajectory.

### 5.1 First part of the HPE

This part lasts approximately between 19:00 UTC 14 October and 05:00 UTC 15 October in the REF simulation.

At 00:00 UTC 15 October, air parcels below 10 km a.s.l. found in the atmospheric column "D" (Fig. 9a) where a convective ~~updraft~~ updraught is simulated originate from 3 preferential directions. Backward trajectories simulated at the end of this first part, e.g. at 04:00 UTC 15 October (not shown), are similar to 00:00 UTC backward trajectories, showing that the latter are representative of this first part.

~~Air parcels~~ Parcels found under 800 m a.s.l. in "D", shown along the axis A–D, are inside the cold sector west of CF1, where virtual potential temperature is below 21 °C (Fig. 9b). They originate from the west, mainly the ~~southeast~~ south-east of the Bay of Biscay and the north of Spain~~. They followed~~ , following the same trajectory as CF1 ~~that was located there at 12:00 UTC 14 October~~ (see Fig. 3c). They ~~remained~~ remain most of the time below 500 m a.s.l., and some ~~were~~ are slightly lifted near CF1 boundary.

Parcels found ~~above~~ between 800 m a.s.l. and 7 km a.s.l. in "D", shown along the axis B–D, are ascending air parcels (Fig. 9c). These parcels originate from east and ~~northeast~~ north-east of the Balearic Islands, over the Mediterranean Sea, away from the convective system ahead of CF2 located between the Balearic Islands and the Pyrenees at 00:00 UTC (Fig. 10c). ~~During their transport over the Mediterranean Sea , the altitude of these parcels remained almost constant~~ They are carried over the Mediterranean Sea by the marine LLJ shown in Fig. 10b and remain at an almost constant altitude between 0 and 1.4 km a.s.l. ~~When they reached the coast, some experienced slight lifting over the Albera Massif and the Corbières Massif but remained below 2 km a.s.l. They were finally lifted up to 6.5 km a.s.l. above CF1. Parcels are carried by the marine LLJ~~

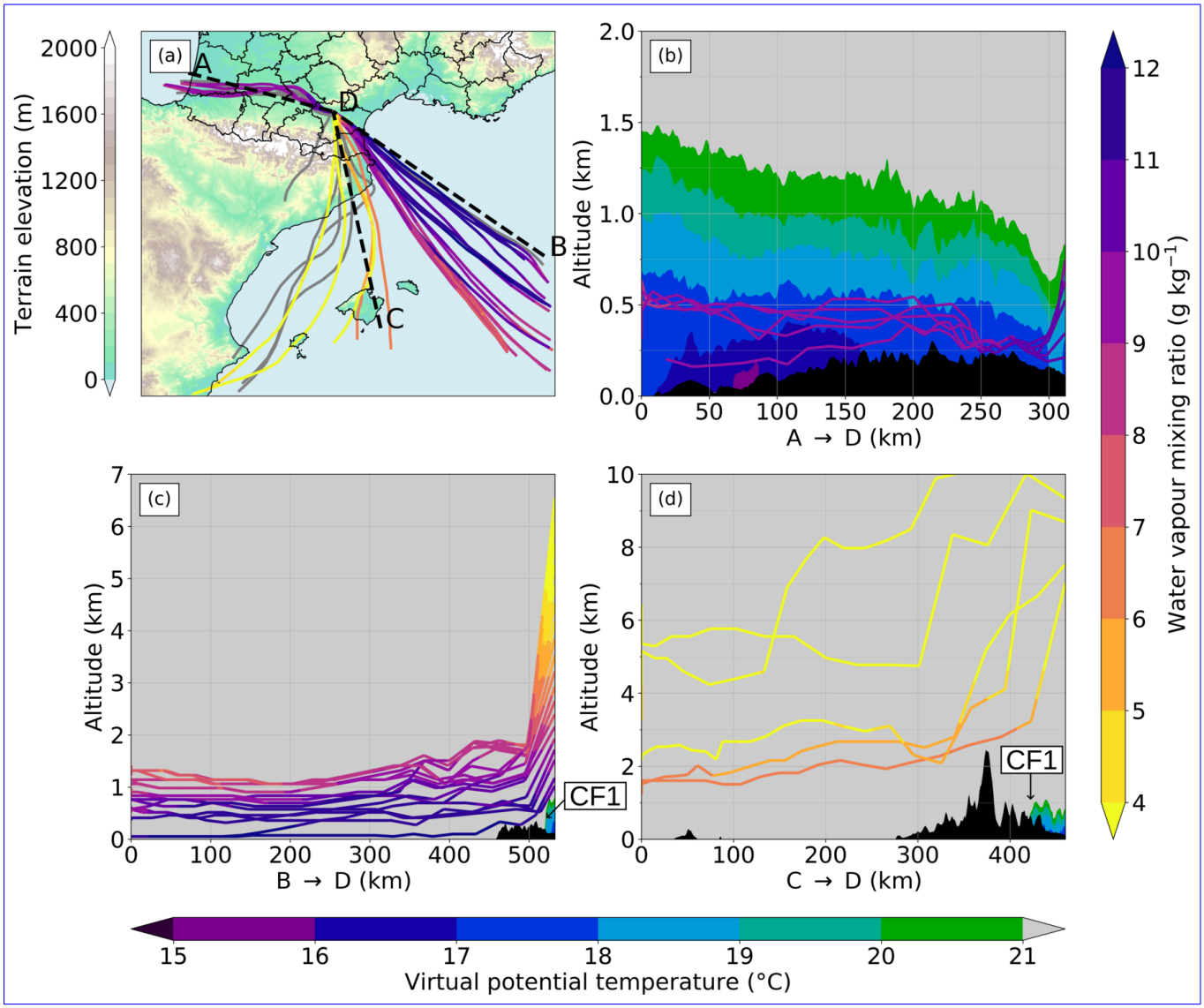


**Figure 9.** (a) Horizontal projection of the 40 backward trajectories from air parcels taken inside the atmospheric column located in "D" (43.25° N, 2.25° E) at 00:00 UTC 15 October in the REF simulation. Trajectories in colour are the ones projected in (b-d): their colour varies according to the water vapour mixing ratio of the parcels. Other trajectories are in grey. Trajectories are computed until 12:00 UTC 14 October, except for parcels that reach domain boundaries before that time. (b-d) Vertical projections of backward trajectories along the dashed black lines shown in (a) and corresponding cross sections of virtual potential temperature at 00:00 UTC 15 October. Each parcel is projected on the section closest to its trajectory inland. Terrain is in black.

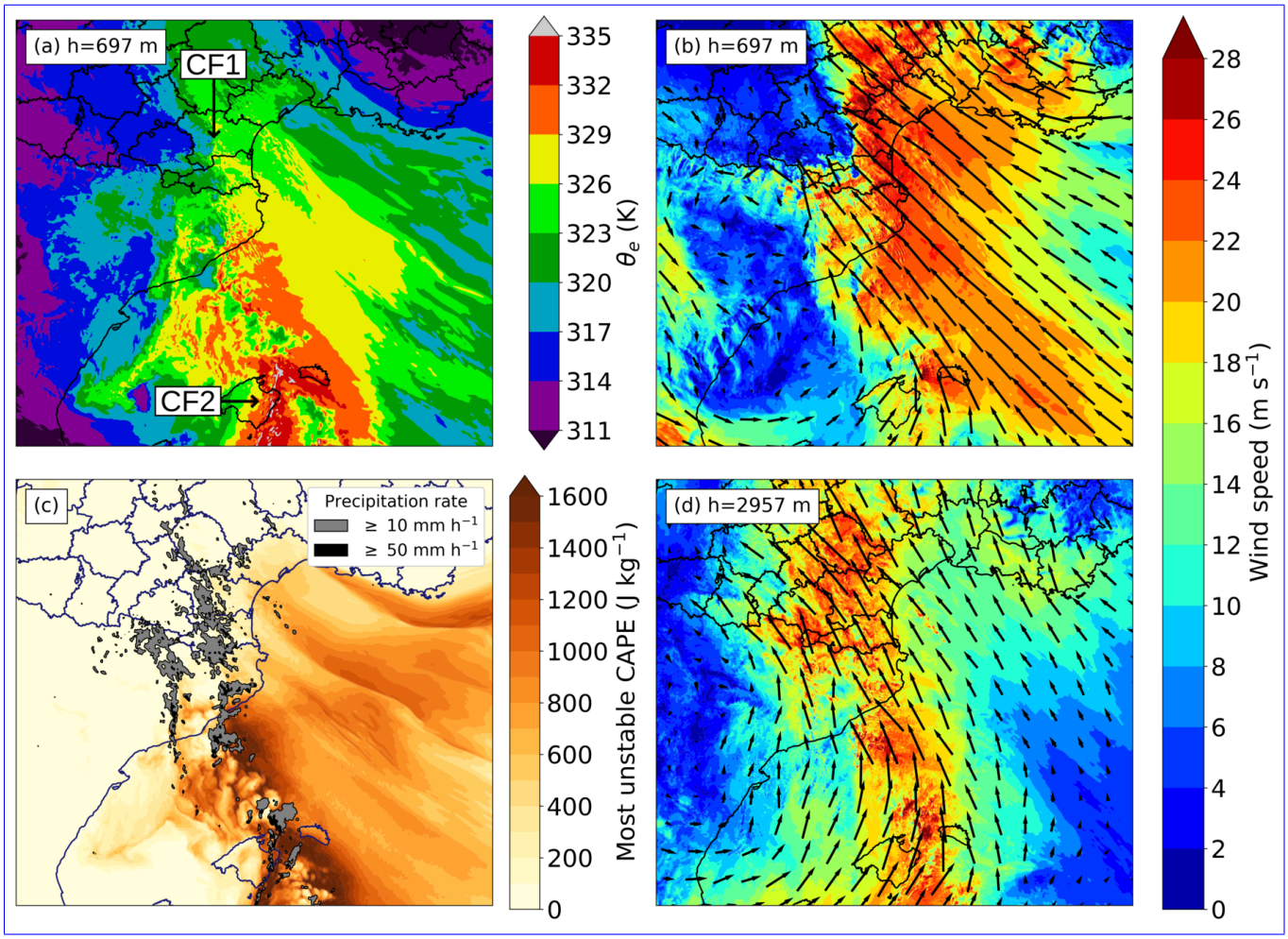


**Figure 10.** REF simulation at 00:00 UTC 15 October of (a) equivalent potential temperature ($\theta_e$) at 697 m height, (b) wind at 697 m height, (c) ~~most unstable CAPE~~ MUCAPE with instantaneous precipitation rate and (d) wind at 2957 m height.

shown in Fig. 10b. At 697 m height, the speed of this southeastern south-eastern LLJ exceeds 20 m s$^{-1}$ between the east of the Balearic Islands and the Aude department, up to 26 m s$^{-1}$ near the Languedoc-Roussillon shore and inland. Such a wind speed transports quickly these air parcels: they travelled travel from B to D (Fig. 9a) in approximately 12 h. When they reach the coast, some experience slight lifting over the Albera Massif and the Corbières Massif but remain below 2 km a.s.l. They are finally lifted up to 6.5 km a.s.l. above CF1. Over the Aude department, large wind convergence is simulated: horizontal wind speed brutally decreases from 26 m s$^{-1}$ to near 0 m s$^{-1}$, leading to enhanced ascending movements along CF1.

These parcels 19 air parcels shown in Fig. 9c originate from moist areas over the Mediterranean Sea (dashed lines in Fig. 4b): at 14:00 UTC 14 October, the 19 air parcels shown in Fig. 9c already had they already have a mean water vapour mixing ratio of 9.1 g kg$^{-1}$ (Tab. 1). Their water vapour mixing ratio increased increase through their transport above the Mediterranean Sea by 1.3 g kg$^{-1}$, reaching 10.4 g kg$^{-1}$ at 20:00 UTC 14 October. During their lifting, between 22:00 and 00:00 UTC, they released release moisture: their water vapour mixing ratio decreased decrease by an average of 4.0 g kg$^{-1}$. Some of this moisture is released through condensation processes inside the convective clouds, before some of the water condensates eventually precipitate. The high moisture and relatively warm temperatures in the area of origin of these parcels is shown in Fig. 10a by equivalent potential temperatures above 5333326 °C K at 697 m height. Consequently, air parcels carried by the LLJ are conditionally unstable: simulated most unstable convective available potential energy (MUCAPE) reaches 100 to 600 J kg$^{-1}$ over Languedoc-Roussillon and 600 to 1200 J kg$^{-1}$ over sea. The 3D CAPE field (not shown) shows convective available potentiel energy (CAPE) field (not shown) indicates that highest CAPE values are mostly reached at the first model level (5 m height), and decrease rapidly with height.

The MSLP low that drives the LLJ is located in the area of light winds over Spain shown in Fig. 10b. Northeast North-east and east of it, between the Balearic Islands and the Pyrenees, strong convective cells are triggered ahead of CF2. Several convective cells are advected by the south-southeasterly south–south-easterly mid-level wind towards Languedoc-Roussillon. Thus, in Fig. 9d some parcels above 7 km a.s.l., shown along the axis C–D, originate from the Mediterranean low and its associated front CF2. These parcels, from altitudes between 1.8 and 5.5 km, have lower water vapour mixing ratios than parcels carried by the LLJ. Some of these parcels are lifted over the Pyrenees mountains and one is lifted over CF1because it managed to cross the Pyrenees without being lifted.

REF simulates southeasterly low-level winds (Fig. 10b a directional wind shear in the lower part of the troposphere: inland, wind veers from east–south-east at 10 m height (not shown) to south-east at 697 m height ) and south-southeasterly mid-level winds (Fig. 10d (Fig. 10b) to south–south-east at 2957 m height ), showing directional wind shear in the lower part of the troposphere. The MSLP trough simulated over the Aude department may locally increase this wind shear inland: Fig. **??**a shows that the LLJ backs from the southeast to the east-southeast inland(Fig. 10d). Backward trajectories confirm it: the higher lower the air parcel comes, the further west east it originates (Fig. 9a).

At 04:00 UTC 15 October, backward trajectories in Fig. **??** picture a situation almost identical to the one from 00:00 UTC. Most of the parcels lifted in the selected updraft are still supplied by the LLJ, coming from altitudes between 0 and 1.2 km for parcels projected along the axis A–D (Fig. **??**b) and between 0.8 and 1.5 km for parcels along the axis B–D (Fig. **??**c). Parcels projected along the axis A–D, coming from the lowest levels supplied large amounts of moisture, slightly increasing during

**Table 1.** Mean water vapour mixing ratio ($g\,kg^{-1}$) of air parcels originating from below 1500 m height along axes shown in Figs. 9,~~??,~~12 as a function of time. Dash indicates that at least one parcel was out of the simulated domain at that time.

| Trajectory end (UTC) | Axis | Number of parcels | Time (UTC) 14:00 | 16:00 | 18:00 | 20:00 | 22:00 | 00:00 | 02:00 | 04:00 | 07:00 |
|---|---|---|---|---|---|---|---|---|---|---|---|
| 00:00 | Fig. 9c: B → D | 19 | 9.1 | 9.6 | 9.9 | 10.4 | 10.1 | 6.1 | | | |
| ~~04:00~~ | ~~Fig. ??b: A → D~~ | ~~8~~ | ~~–~~ | ~~–~~ | ~~–~~ | ~~10.5~~ | ~~10.8~~ | ~~11.0~~ | ~~11.0~~ | ~~5.7~~ | |
| 07:00 | Fig. 12b: A → B | 7 | – | – | – | – | – | 8.6 | 9.8 | 10.4 | 5.3 |

~~their transport from 10.5 to 11.0 g kg$^{-1}$ between 20:00 and 02:00 UTC (Tab. 1). These parcels were lifted up to 7 km a.s.l. immediately above CF1. Most of the air parcels along the axis B–D had a similar path and were lifted up to 8 km a.s.l., except two parcels that were lifted above the orography near 650 km along B–D. Only few elevated parcels came from the Balearic Islands, i.e. from inside the convective system ahead CF2. They were lifted above the Pyrenees (Fig. ??d) and reached levels above 9 km a.s.l. in column "D" with a water vapour mixing ratio before they reached the column lower than 4 g kg$^{-1}$.~~

## 5.2 Second part and end of the HPE

This part lasts approximately between 05:00 and 10:00 UTC 15 October in the REF simulation ~~. Around 05:00 UTC, the~~ and begins when the rain band associated with the cold front CF2 ~~reached the Pyrénées-Orientales~~ reaches the Pyrenees-Orientales coast. Contrary to the first part during which most of convection is triggered inland, in this second part, convection is triggered over the Mediterranean Sea (Fig. 11c) and carried inland by the mid-level wind (see wind around 3 km height in Fig. 11d), diminishing the influence of local forcings in triggering convection. Convection triggered over sea is fed by a warm and moist air mass ahead of CF2 with equivalent potential temperature up to ~~59~~332 ~~°C~~ K (Fig. 11a). Consequently, this air mass is more unstable than in the first part: ~~MUCAPE values simulated~~ simulated MUCAPE values are up to 1600 J kg$^{-1}$ (Fig. 11c).

At 07:00 UTC an increasing number of air parcels found inside ~~updrafts~~ updraughts over the Aude department originate from south of the Balearic Islands, i.e. ~~directly~~ from CF2, the front formed with Leslie's remnants (Fig. 12a) in comparison with the first part. These parcels, projected in Fig. 12c originate from altitudes between 1 and 4 km, ~~generally higher than what was simulated~~ altitudes generally higher than in the first part. Some air parcels carried by the LLJ, coming from the east of the domain ~~and~~ at altitudes between 0 and 1 km are still found ~~and projected in Fig. 12b. If their number decreased (Fig. 12b). If their number decreases~~ compared to the first part, their ~~water vapour mixing ratio remains high with~~ average water vapour mixing ratio of 10.4 g kg$^{-1}$ ~~on average, which increased~~ remains high and increases through their transport above the Mediterranean Sea by 1.8 g kg$^{-1}$ (Tab. 1). Some descending dry air parcels are also found ~~(Fig. 12d), originating~~ to originate from dry mid-level areas located at the rear of CF2 ~~.~~ (Fig. 12d).

In the lower levels, at 697 m, REF simulates a strong wind variation along CF2~~(Fig. 11b)~~: ahead of CF2, the ~~southeasterly~~ south-easterly LLJ reaches 22 to 26 m s$^{-1}$ while at the rear wind turns ~~southwesterly~~ south-westerly and only reaches 6 to 12 m s$^{-1}$ ~~.~~ (Fig. 11b). Between 07:00 ~~UTC~~ and 09:30 UTC, the ~~northeastwards~~ north-eastwards advance of CF2 ~~propagated~~

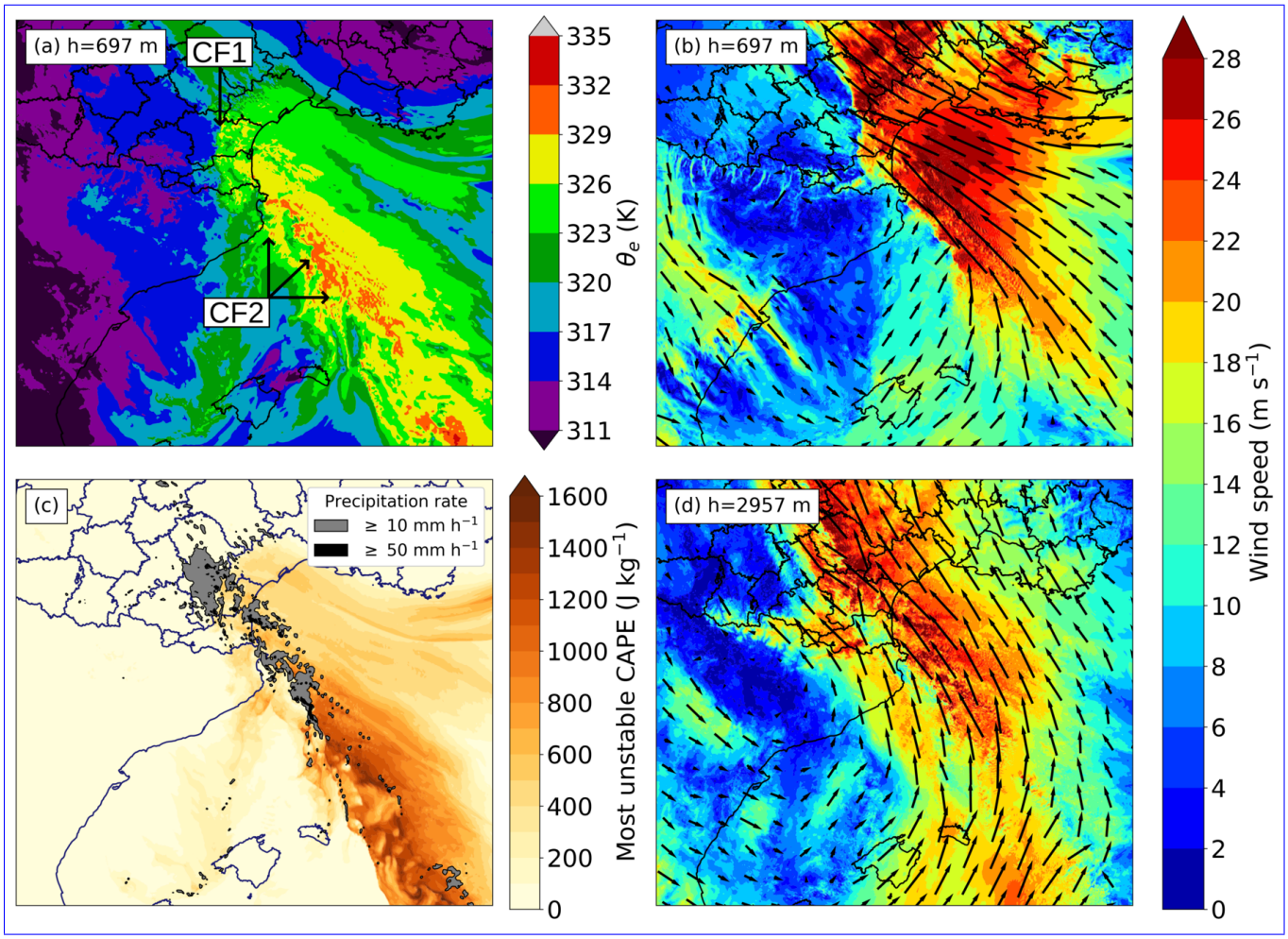


**Figure 11.** As Fig. 10 at 07:00 UTC 15 October.

propagates this wind variation over the Aude department ~~. When wind speed decreased~~ (not shown). When wind speed abruptly decreases along CF1, CF1 stationarity breaks and the cold air west of CF1 ~~started flowing eastwards , towards the Mediterranean Sea, as a density current, spreading out circularly over the sea. This cold air rapidly flowing as soon as the LLJ stops tends to show that an equilibrium maintaining~~ immediately starts flowing eastwards in a similar manner to a density current, and later spreads out circularly over the Mediterranean Sea (not shown). It indicates that, during the HPE, the propagation of the cold air located west of CF1 ~~quasi-stationary was reached between CF1 and the LLJ . Then, the equilibrium progressively broke from south to north by the advance of CF2~~is countered by the LLJ blowing perpendicularly to it, also in a similar manner to the propagation of a cold pool can be countered by the environmental wind (Miglietta and Rotunno, 2014).

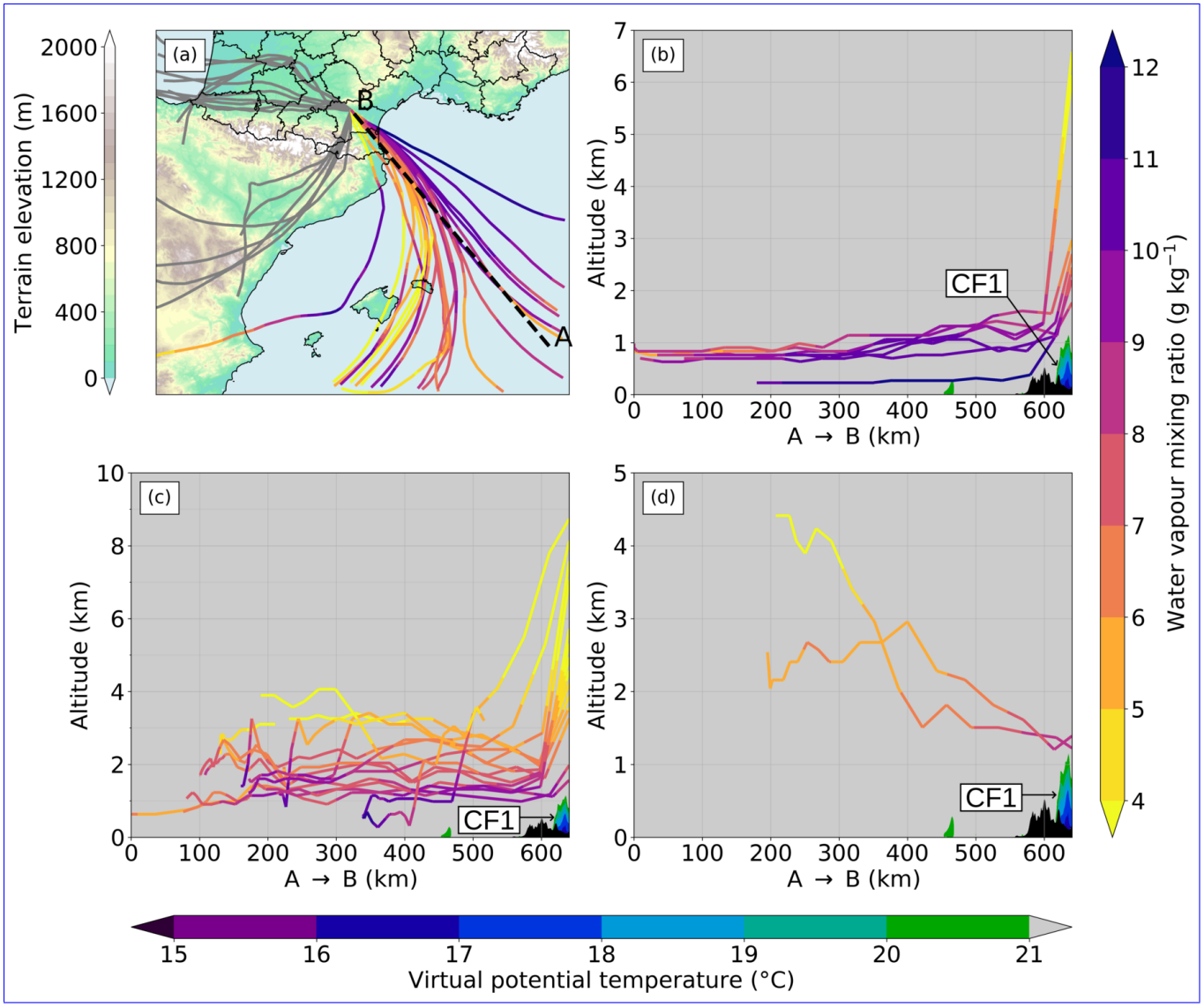


**Figure 12.** As Fig. 9 for trajectories ending at 07:00 UTC 15 October at 43.26° N, 2.34° E. Air parcels are projected along the same axis A–B but separated depending on their origin and behaviour: (b) ascending parcels from east, (c) ascending parcels from south or west and (d) descending parcels from south.

**Table 2.** Properties and geographic origin of air parcels found in the atmospheric column $C_{338}$ as a function of time, aggregated in time intervals from 19:00 UTC 14 October to 10:00 UTC 15 October. Mean water vapour mixing ratio 2 h before reaching $C_{338}$ (i.e. before some parcels are lifted) is indicated by $\bar{r_v}$.

| Initial parcel location | Properties | Time interval (hours in UTC) | | | | | | |
|---|---|---|---|---|---|---|---|---|
| | | [~~19–21~~19,21[ | [~~21–23~~21,23[ | [~~23–01~~23,01[ | [~~01–03~~01,03[ | [~~03–05~~03,05[ | [~~05–07~~05,07[ | [~~07–09~~07,09[ |
| East of 4.5° E | Number | **76** | **67** | **76** | **70** | **75** | **52** | 25 |
| | $\bar{r_v}$ (g kg$^{-1}$) | 10.6 | 9.7 | 9.4 | 9.4 | 8.7 | 9.0 | 10.2 |
| West of 4.5° E – south of 42° N | Number | 66 | 55 | 48 | 33 | 31 | 39 | **64** |
| | $\bar{r_v}$ (g kg$^{-1}$) | 2.6 | 1.7 | 3.7 | 4.6 | 4.8 | 4.9 | 4.7 |
| Other | Number | 2 | 22 | 20 | 41 | 38 | 53 | 55 |
| | $\bar{r_v}$ (g kg$^{-1}$) | 9.6 | 9.9 | 10.2 | 9.6 | 9.3 | 8.9 | 8.9 |

### 5.3 Amount of moisture supplied by Leslie's remnants

To quantify the amount of moisture brought over the Aude department during the HPE by Leslie's remnants, the geographic origin of air parcels found in the atmospheric column above the 338 mm precipitation maximum simulated by REF (see Fig. 6b, now referred to as $C_{338}$) is tracked. Every 30 min from 19:00 UTC 14 October to 10:00 UTC 15 October (the time period of the HPE in the REF simulation), backward trajectories of 36 air parcels taken every 2 vertical levels of the model between 18 m and ~~9924~~about 10 ~~m height are computed until 12:00 UTC 14 October,~~ km height are computed until the beginning of the REF simulation. Here, parcels above 10 km height are not taken because most parcels followed above this height are not found inside any ~~updraft~~ updraught over the Aude department.

The computation of backward trajectories provides the initial parcel location: it is ~~the location of the parcel~~ either its location at 12:00 UTC 14 October or where the parcel enters the parent domain if the parcel is out of the ~~parent domain at that time, it is the location where the parcel enters the parent domain~~domain at that time. The geographical origin is divided in 3 categories (Tab. 2): east of 4.5° E, west of 4.5° E – south of 42° N ~~and other. Such division is done because~~ corresponding to air parcels from Leslie's remnants~~originate from the area west of 4.5 E – south of 42 N~~, and other. The "other" category includes mostly ~~cold and stable air parcels. These parcels are found at the lowest levels of the atmospheric column because it is~~ low-level cold and stable air parcels located west of CF1 (~~such parcels are shown in~~ Fig. 9b). Because these parcels are stable, only the first categories including conditionally unstable air parcels are compared.

Tab. 2 shows that 42 % of air parcels found in $C_{338}$ ~~originated~~ originate from east of 4.5° E, i.e. from east of the Balearic Island, and they ~~carried~~ carry 54 % of the water vapour mixing ratio of all air parcels tracked. On the contrary, 34 % of air parcels coming from Leslie's remnants ~~carried~~ carry only 17 % of the water vapour mixing ratio ~~, although their number particularly increased~~ of all air parcels tracked, although their number particularly increases in the second part of the event. This result suggests that air parcels ~~coming from east of 4.5 E, over the Mediterranean Sea, supplied~~ originating from the Mediterranean Sea, east of the Balearic Islands, supply more moisture to convective cells than air parcels originating from Leslie's remnants.

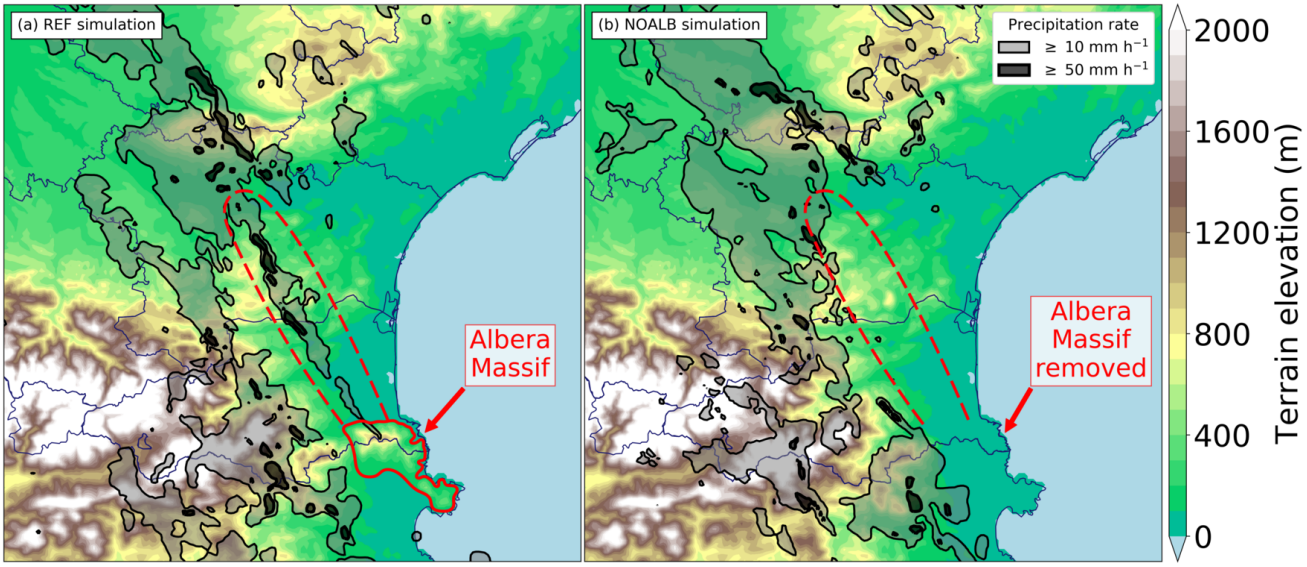


**Figure 13.** Instantaneous precipitation rate at 05:00 UTC 15 October superimposed on the terrain elevation of (a) REF and (b) NOALB simulations.

### 5.4 Lifting by the Albera Massif and effect on precipitation

To understand the role of the Albera Massif in generating convective bands downwind, as it is observed and simulated by REF, the simulations REF and NOALB are compared.

Heavy precipitation is simulated by REF at 05:00 UTC over the highest slopes of the Albera Massif and along a line downstream of the massif (Fig. 13a, dashed red area). When the Albera Massif is removed ~~, Fig. 13bshows that~~ in NOALB (Fig. 13b), no precipitation is simulated over or downstream of it. ~~In NOALB~~Also, along the eastern Pyrenees, west of the dashed red line, a slightly larger area of instantaneous precipitation above 10 mm $h^{-1}$ is found than in REF. ~~Fig. 14a shows that over~~ Over and downstream of the Albera Massif, heavy precipitation in REF results from aligned convective cells exhibiting ascending vertical velocities above 4 m $s^{-1}$ (Fig. 14a), whereas no substantial ascending movement is found along this line in NOALB (Fig. 14b). The orientation of the line of ~~updrafts~~ updraughts (along the A–B axis in Fig. 14a) is parallel to the horizontal wind streamlines at 2674 m height, showing that convective cells are aligned with the ~~south-southeastern~~ south–south-eastern mid-level wind direction. Superimposed with this line of ~~updrafts~~updraughts, lee waves resulting in quasi-stationary, evenly spaced, ~~couples~~ couplets of positive and negative vertical velocities ~~indicated by the large black arrows in Fig. 14aare simulated by REF~~ are simulated by REF (Fig. 14a,large black arrows) but are not found in NOALB (Fig. 14b).

To quantify the flow regime of the situation at 05:00 UTC 15 October, the mountain Froude number $\mathrm{Fr_m} = \frac{U}{Nh}$ (Kirshbaum et al., 2018) is estimated, where U is the mean wind speed of the layer, N is the Brunt-Väisälä frequency and h is the mountain height. Here h = 1128 m, the maximum height of the Albera Massif in the model. To compute N, the bulk method de-

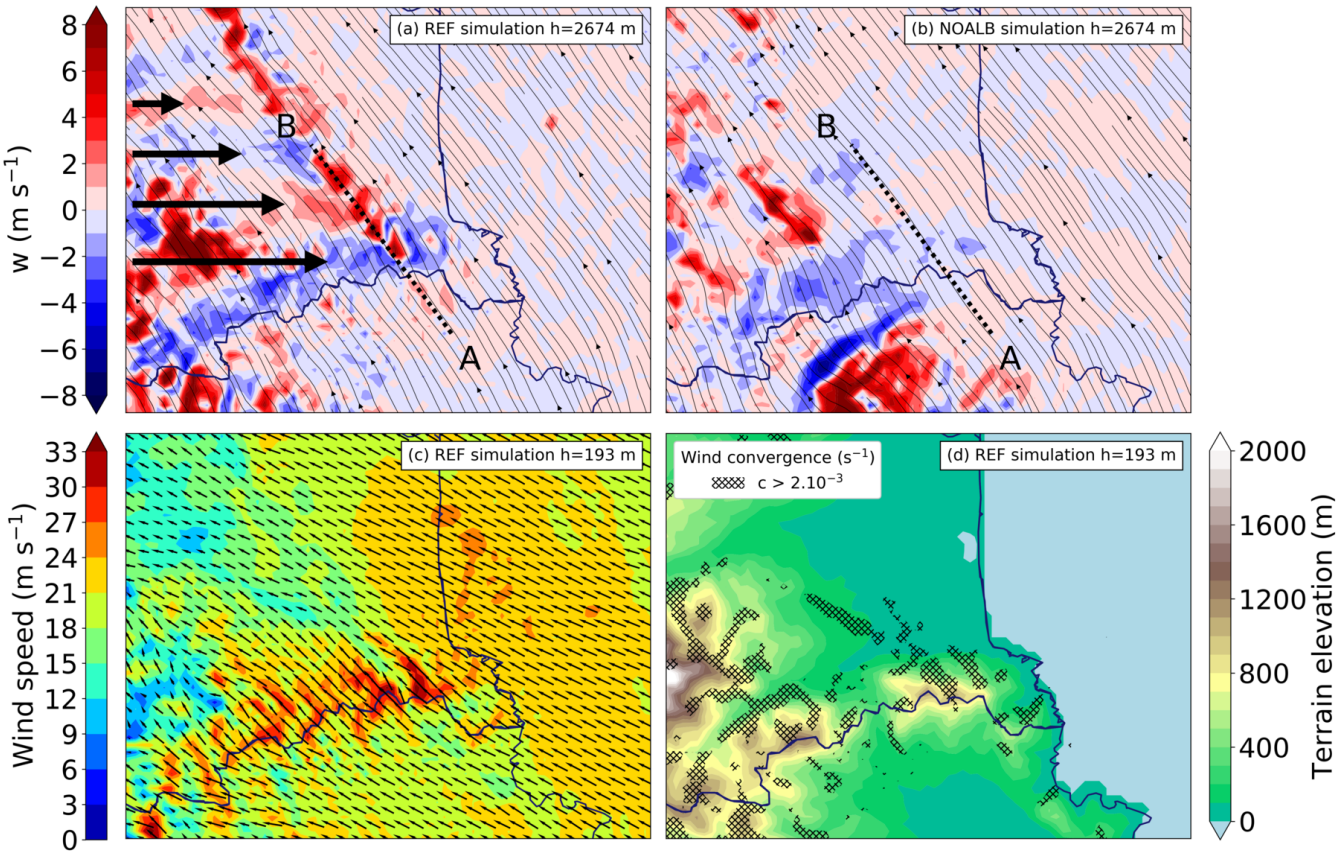


**Figure 14.** Vertical velocity (w) and horizontal wind streamlines at 2674 m height in the (a) REF and (b) NOALB simulations. Horizontal wind (c) speed and direction and (d) convergence $> 2 \times 10^{-3}$ s$^{-1}$ at 193 m height in the REF simulation at 05:00 UTC 15 October.

scribed by Reinecke and Durran (2008) is used considering a single layer which has approximately the height of the mountain: ~~$N = \sqrt{\frac{g}{\theta}\frac{\theta_{(25)}-\theta_{(1)}}{h}}$~~ $N = \sqrt{\frac{g}{\bar{\theta}}\frac{\theta_{(25)}-\theta_{(1)}}{h}}$, where $g = 9.81\,\mathrm{m\,s^{-2}}$ is the standard acceleration of gravity, $\theta_{(n)}$ is the potential temperature at model level n (first level is at 5 m height and the 25$^{th}$ is at 1143 m height) and $\bar{\theta}$ is the mean potential temperature over the layer. The moist Froude number $Fr_w = \frac{U}{N_w h}$ (Chen and Lin, 2005) is also computed, where $N_w$ is the moist Brunt-Väisälä frequency that differs from N because $\theta$ is replaced by $\theta_v$. The computation of U, N and $N_w$ is an average over 100 grid points located upwind the mountain, precisely the grid points less than 10 km east and 10 km south of grid point A (A is shown in Fig. 14a). Computation leads to $U = 21.3\,\mathrm{m\,s^{-1}}$, $N = 9.9 \times 10^{-3}\,\mathrm{s^{-1}}$, $N_w = 8.9 \times 10^{-3}\,\mathrm{s^{-1}}$ which gives $Fr_m = 1.9$ and $Fr_w = 2.1$. According to Kirshbaum et al. (2018), $Fr_m = 1.9 > 1$ indicates that the flow tends to directly ascend the terrain over the windward slope instead of being deflected around the obstacle. This ascent mechanically lifts the conditionally unstable air parcels supplied by the LLJ, but also ~~probably~~ likely triggers the aforementioned lee waves. $Fr_w = 2.1$ corresponds to the flow regime IV of Chen and Lin (2005), described as a flow with an orographic stratiform precipitation system over the mountain and

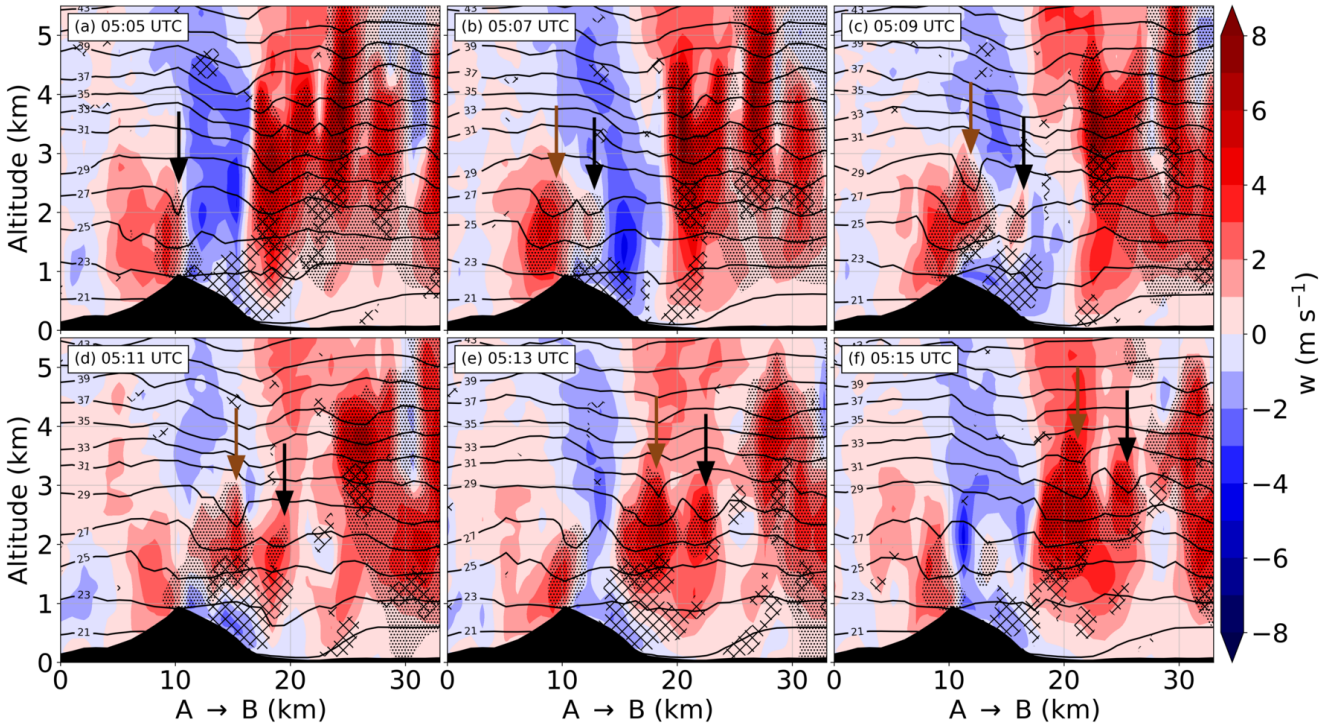


**Figure 15.** Vertical velocity (w, m s$^{-1}$), potential temperature (black contours, °C), horizontal convergence > 2 × 10$^{-3}$ s$^{-1}$ (black diagonal hatches) and hydrometeor mixing ratio > 1 g kg$^{-1}$ (little black dots) between 05:05 and 05:15 UTC 15 October. Terrain is in black.

possibly a downstream-propagating cloud system (a stratiform cloud is defined by the authors as having a cloud depth less than 4 km)~~precipitation system over the mountain and possibly a downstream-propagating cloud system~~.

To closely look at how convective cells are initiated and maintained, a time evolution of the vertical cross section A–B simulated by REF is shown in Fig. 15. At 05:05 UTC, a convective cell containing hydrometeors is formed above the Albera Massif (Fig. 15a, black arrow). Inside this cell, the potential temperature is higher than the environment around 2 km height probably due to latent heat release associated with water phase changes. This cell is advected towards B by the mid-level wind. A second cell is initiated at the rear of the first one by orographic lifting and the surface of hydrometeor mixing ratio above 1 g kg$^{-1}$ ~~has rapidly increased~~ rapidly increases (Fig. 15b, brown arrow). On the lee side of the mountain, these convective cells propagate in the middle of a large subsidence area (related to the aforementioned lee wave)~~, but it seems that counteracting the effect of the subsidence,~~ . Subsidence appears counteracted by a quasi-stationary wind convergence zone located near the ground ~~connects with the updrafts~~ which connects with the updraughts and invigorates them. This wind convergence zone is simulated downwind of the mountain (Fig. 14d) and seems due to rapid wind decrease and some wind confluence in the lee side of the Albera Massif (Fig. 14c). Then, as shown by Figs. 15d,e, both cells connect with an ascending zone of the lee wave around 20 km along the axis A–B and rapidly grow: the hydrometeor mixing ratio surface above 1 g kg$^{-1}$ as well as the

vertical velocity are found to rapidly increase inside both cells. These findings are consistent with the description of the flow regime IV of Chen and Lin (2005): vertical velocities above 1 m $s^{-1}$ and hydrometeor mixing ratios above 1 g $kg^{-1}$ remain below 4 km~~altitude~~ a.s.l. over the mountain, and convective cells ~~are propagating~~ propagate downstream of the mountain.

Because of the ~~slightly~~ slight directional vertical wind shear simulated in the lower part of the troposphere (see wind direction in Figs. 14a,c), ~~the LLJ continuously supplies conditionally unstable air parcels to the convective cells formed from their southeastern flankwhile these cells are advected by the south-southeastern~~ once convective cells are on the lee side of the mountain, as they are advected by the south–south-eastern mid-level ~~wind~~wind, the south-eastern LLJ supplies conditionally unstable air parcels that do not cross the Albera Massif to the cells from their south-eastern flank. Backward trajectories starting from their ~~updrafts (not shown) show that once convective cells are on the lee side of the mountain, as they are advected north-northwestwards, an increasing~~ updraughts (not shown) indicate that the number of low-level moist air parcels that ~~have not crossed the Albera Massif are found inside the cells . Thus, the supply of conditionally unstable air parcels along the line is continuous and~~ do not cross the Albera Massif found inside the cells increases as they are advected. This supply mechanism possibly explains the maintenance of the convective cells long after they are formed.

This preferential organization of convection along a line downstream of the Albera Massif results in substantial departures in 24 h rainfall accumulations between NOALB and REF (Figs. 6b,d)~~between NOALB and REF. Precipitation along the band downstream of the Albera Massif called eastern band in Sect. 2~~. Precipitation along the eastern band (see Sect. 2), downstream of the Albera Massif, is reduced by as much as 100 mm in NOALB compared to REF. REF maximum precipitation over plains is reduced from 338 ~~mm~~ to 310 mm, and the maximum in NOALB (332 mm) is shifted over mountains. Concomitantly, precipitation is enhanced along the western ~~precipitation band (see Sect. 2)~~ band downstream of the eastern slopes of the Pyrenees: maximum precipitation is increased from 296 ~~mm~~ to 327 mm in NOALB compared to REF. Precipitation is also enhanced between both bands, along the quasi-stationary CF1. Consequently, the ~~southeast-northwest~~ south-east–north-west orientation of the precipitation zone exceeding 240 mm in REF is replaced by a ~~south-north~~ south–north orientation in NOALB.

This sensitivity experiment shows the large importance of the Albera Massif in the shape of the precipitation field, focusing precipitation downstream of it while reducing precipitation elsewhere. The proposed mechanism describing convection initiation over the Albera Massif, ~~one of the~~ first relief intercepting the marine LLJ, and the convective cells maintenance downstream of ~~these~~ the Albera Massif may be applied to similar reliefs. ~~It may explain the enhanced amount of precipitation observed along the western band and the formation of the third line starting over the~~ Additional simulations (not shown) in which the Corbières ~~Massif observed between 00:00 and 02:00~~Massif and the Eastern slopes of the Pyrenees are successively flattened show a substantial decrease in maximum accumulated precipitation downstream of these reliefs, associated with a spread of precipitation above 200 ~~UTC (Fig. 5c).~~ mm over a larger area along the quasi-stationary front.

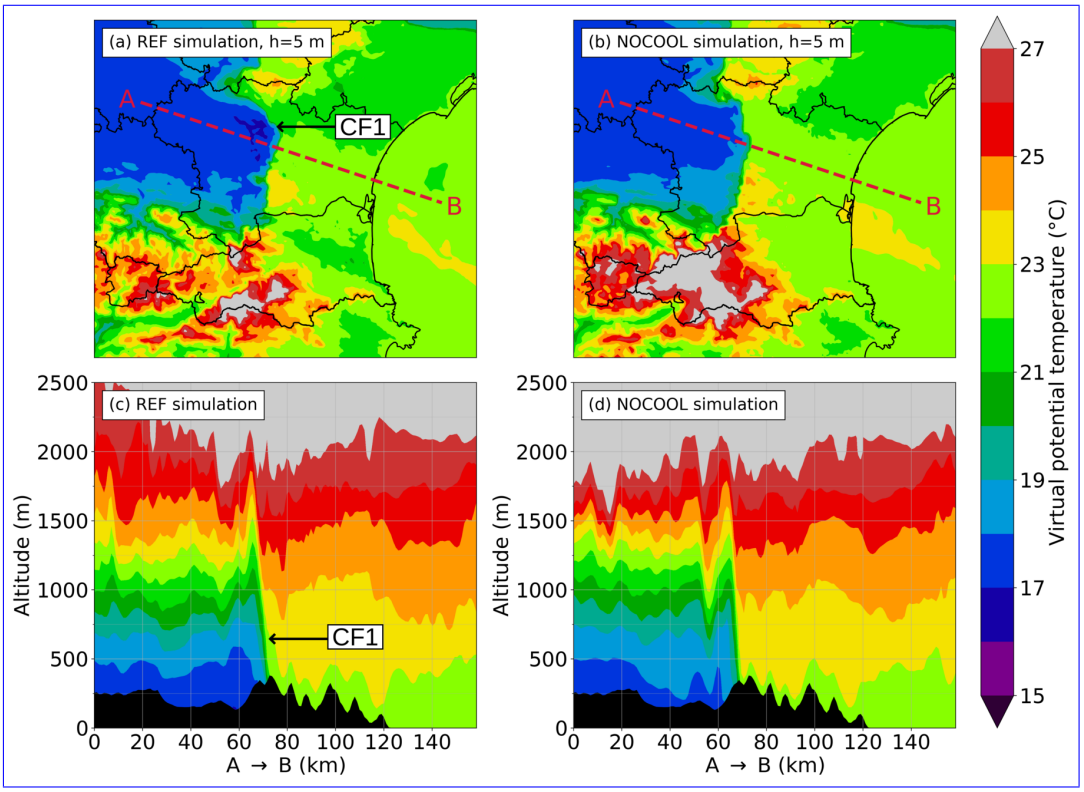


**Figure 16.** Virtual potential temperature at 5 m height for the (a) REF and (b) NOCOOL simulations at 04:00 UTC 15 October. Vertical cross sections of virtual potential temperature along the A–B axis are drawn for the (c) REF and (d) NOCOOL simulations.

## 6 Influence of the cooling associated with the evaporation of precipitation

This section investigates the possible influence of the cooling associated with the evaporation of precipitation over the Aude department on CF1. The following questions are addressed. Does this process (i) modify the location of CF1? (ii) extend the duration of CF1 stationarity? (iii) enhance the temperature gradient along CF1?

~~Fig. 6c shows the resulting~~ Regarding 24 h accumulated precipitation~~observed in the NOCOOL simulation. Precipitation~~ , it is globally higher in NOCOOL than in REF ~~, maximum~~ while remaining organized in two major bands whose orientation is slightly rotated clockwise compared to REF (Figs. 6b,c). Maximum precipitation reaches 415 mm in NOCOOL and only 338 mm in REF. ~~Compared to REF, a local maximum of precipitation of 310 mm located north-northwest of the global maximum appears in NOCOOL. The organization of the precipitation in two major bands remains but their orientation is slightly rotated clockwise compared to REF.~~

At 04:00 UTC, both REF and NOCOOL exhibit a sharp ~~east-west horizontal~~ east–west virtual potential temperature ($\theta_v$) gradient that delineates the location of CF1 (Fig. 16). At 5 m height, REF shows about 0.5 to 1 °C colder temperatures than NOCOOL on both sides of CF1. Highest departures are found over the Pyrenees. South of the A–B axis, CF1 is shifted from

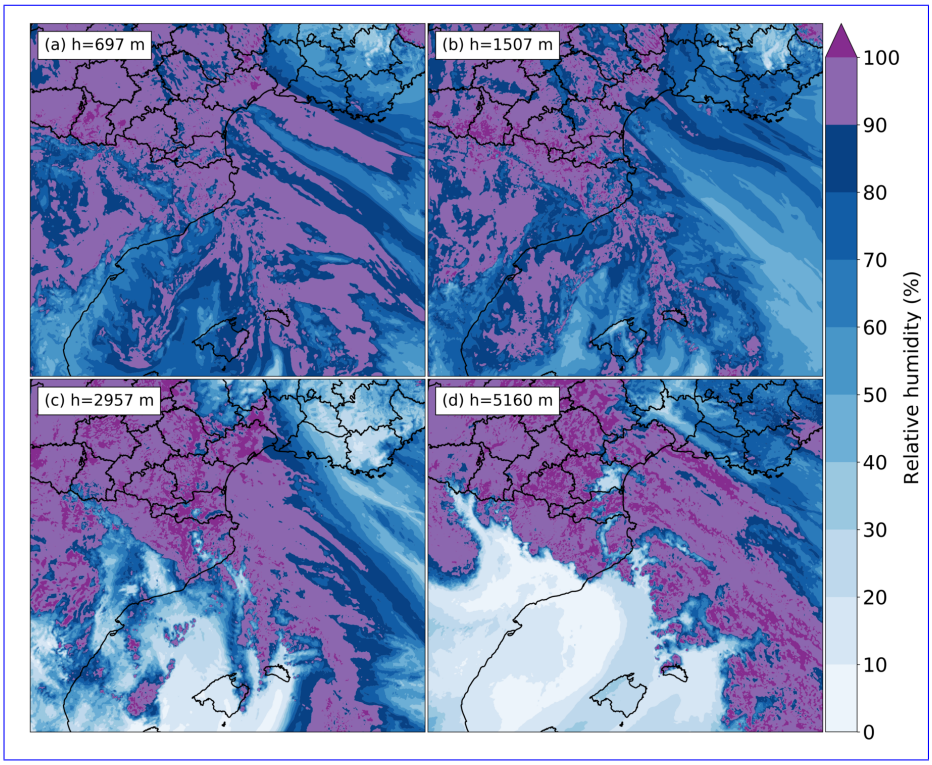


**Figure 17.** Relative humidity in the REF simulation at 04:00 UTC 15 October at (a) 697 m height (b) 1507 m height (c) 2957 m height (d) 5160 m height.

0 to 10 km west in NOCOOL compared to REF, depending on the latitude. Along the A–B axis ~~, vertical cross sections of~~ (Figs. 16c,d~~show that~~ ), near the ground, CF1 is ~~about 90~~very close between REF and NOCOOL: it is only about 4 km ~~from A in NOCOOL and 87 km from A in REF, near the ground~~further west in NOCOOL than in REF. The $\theta_v$ gradient is visible up to 2 km~~in both simulations. East of CF1, near the ground, virtual potential temperatures of about 22 °C are found in both simulations. West of CF1, these temperatures are only found at altitudes between 1000 and 1500 m in REF and between 875 and 1400 m in NOCOOL. West of CF1, inside the cold air, the altitude of the isotherm $\theta_v$ = 18 °C is higher in REF with about 450 m than in NOCOOL with about 325 m. Above 750 m~~ a.s.l. ~~, the vertical temperature gradient is stronger in NOCOOL than in REF, thus REF shows slightly lower temperatures than NOCOOL from 750 to 2500 m.~~

~~Along the A–B axis~~in both simulations. East of CF1, departures of generally less than 0.5 °C are found between simulations~~east of CF1~~. West of CF1, generally higher ~~temperatures~~ $\theta_v$ are found in NOCOOL compared to REF, with ~~temperatures~~ NOCOOL up to 2 °C higher ~~found in NOCOOL~~ than REF near A above 1500 m~~and near B.Near CF1 and near the ground, departures remain generally below 1 °C.~~ a.s.l.

The evaporative cooling does not shift the location of CF1 by more than few kilometres or substantially modify the ~~temperature~~ $\theta_v$ gradient along it. Comparison of REF and NOCOOL does not show any extended duration of CF1 station-

arity or substantial time lag between simulations. However, ~~globally higher temperatures are~~ higher $\theta_v$ simulated in NOCOOL than in REF ~~in the lowest troposphere because evaporative cooling is switched off. These higher temperatures result in globally higher MUCAPE (not shown)~~ are explained by the evaporative cooling switched off. These higher $\theta_v$ result in globally higher MUCAPE and consequently stronger convective cells and stronger rain rates in NOCOOL than in REF ~~. This probably~~ (not shown). This difference possibly explains why precipitation is substantially higher in NOCOOL than in REF ~~.~~ (Figs. 6b,c).

One of the reasons ~~that may have limited the~~ for the small evaporative cooling west of CF1, where highest precipitation is observed, is the small evaporation due to near saturation of air masses in the lower troposphere according to the REF simulation (Fig. 17). At 04:00 UTC, relative humidity ~~exceeded~~ exceeds 90 % over most of Languedoc-Roussillon and a dry air mass ~~was~~ is only found over Spain, at the rear of CF2. ~~Large evaporative cooling associated with dry levels between 1000 and 4000 m is not simulated in this case. Such difference may explain why the location of CF1 between REF and NOCOOL is similar. The~~ The fact that the cooling associated with evaporation processes does not have any substantial impact on the stationarity of the simulated MCS ~~on the 2018 Aude HPE , agreeing~~ in this HPE agrees with the same observation of Ducrocq et al. (2008) ~~on~~ for the 1999 Aude HPE.

## 7 Conclusions

The ~~meteorological situation of the~~ synoptic situation on 14 and 15 October 2018 ~~exhibited favourable ingredients leading~~ was favourable to a HPE over Languedoc-Roussillon~~and particularly the Aude department. The remnants of the former hurricane Leslie are~~ . The remnants of hurricane Leslie were involved in the formation of a Mediterranean surface low and its associated cold front (CF2). The rapid deepening of this ~~Mediterranean~~ surface low, extended by a trough over Languedoc-Roussillon, contributed to strengthen a low-level jet (LLJ) over the Mediterranean Sea. Meanwhile, a decaying cold front (CF1) remained quasi-stationary in the middle of the Aude department, west of the trough. The slow movement northwards of the ~~Mediterranean~~ surface low as well as the quasi-stationarity of ~~its associated~~ the trough sustained quasi-stationary atmospheric conditions ~~during several hours over the Aude department, while continuously supplying conditionally unstable air parcels over the area~~that continuously supplied conditionally unstable air parcels during several hours over the Aude department.

A two-way grid nested numerical simulation at 1 km and 500 m horizontal resolutions ~~was successfully~~ is carried out with the Meso-NH model~~with initial and boundary conditions provided by the operational AROME analyses every 3 h. A comparison of the simulation with~~ . The realism of this simulation is assessed using in particular near-surface analyses built from observations of standard and personal weather stations~~was performed~~. Compared to observations, the simulation delays ~~by approximately 3 h the arrival of the precipitation system~~ the arrival of precipitation ahead of CF2 over the Aude department as well as the end of the HPE over the west of this department. ~~The~~ Also, the location where both CF1 and the trough ~~remained~~ remain quasi-stationary is well simulated ~~, around 10 km farther west than in analyses,~~ but the stationarity duration of both low-level mesoscale boundaries is ~~overestimated by 3 to 4.5 h. Simulated~~ longer than observed. Consistent with these longer stationarities and the delay, simulated 24 h accumulated precipitation is ~~found realistic but slightly overestimatedcompared to observations. This overestimation is consistent with the delay that caused longer precipitation over the Aude department.~~

~~Despite these differences, the simulation is considered realistic enough and taken as the reference (REF) to study the case.~~ slightly overestimated.

The ~~study~~ simulation reveals that the main origin of lifted air parcels and dominant mechanisms that ~~triggered convection~~ differ ~~during the two parts of this HPE.~~

~~The first partbegins around 19:00 UTC 14 October in both observations and the REF simulation. In this part, the REF simulation shows that conditionally unstable air parcels originating from the Mediterranean Sea, east of the Balearic Islands~~trigger convection differ during the HPE. In a first part, conditionally unstable air parcels mainly originate from east of the Balearic Islands, over the Mediterranean Sea, at altitudes between 0 and 1.5 km. They are carried by the LLJ towards the Languedoc-Roussillon shore ~~. During their transport above the Mediterranean Sea, inside the model's domain, the water vapour mixing ratio of the tracked air parcels increases by 0.5 to 1.8 g kg$^{-1}$~~while moistened during their transport over the Mediterranean Sea. Once inland, these air parcels are continuously lifted over the upwind slopes of the first mountains encountered, i.e. mostly eastern Pyrenees relief, the Albera Massif and the Corbières Massif. ~~Both observation and simulation show that convective~~ Convective cells organize along quasi-stationary lines downwind of the mountains, forming the active parts of a back-building MCS. ~~Convective cells appear to be~~ Cells are maintained and reinforced downwind of the terrain by low-level leeward convergence, ascending areas created by mountain lee waves and favoured supply in conditionally unstable air due to the low-level directional wind shear. ~~Indeed, formed cells are continuously advected north-northwestwards by the mid-level wind while the LLJ supplies conditionally unstable air on their southeastern side.~~ A sensitivity study shows that the convective line downwind of the Albera Massif disappears when the Albera Massif terrain is flattened, ~~showing~~ revealing the crucial role of terrain in the formation of these lines. ~~Convection is particularly enhanced above and west of the quasi-stationary cold front CF1, along which a strong wind convergence line as well as a substantial virtual potential temperature gradient are simulated and observed. Most parcels found in large updrafts near the simulated precipitation maximum, west of CF1, are found to be lifted above CF1.~~

~~The second partbegins around 02:00 UTC 15 October in observations and 05:00 UTC in the REF simulation. In this part, the REF simulation shows that~~ In a second part, an increasing number of conditionally unstable air parcels originates from south of the Balearic Islands i.e. from the vicinity of the Mediterranean surface low and CF2 ~~, both formed with Leslie's remnants,~~ at altitudes mostly between 1 and 4 km. ~~The advance of CF2 and~~ Convective cells are triggered within the conditionally unstable air mass located ahead of ~~it trigger convective cells over the Mediterranean Seathat are~~ CF2, over the Mediterranean Sea, and advected towards the Languedoc-Roussillon coast. Inland, the MCS loses progressively its organization in lines~~in this second part and the strongest rain rates are found along and west of CF1~~. The end of the HPE ~~over the Aude department~~ is driven by the advance of CF2 ~~northeastwards~~north-eastwards.

Throughout the event, convection is particularly enhanced above and west of the quasi-stationary front CF1, whose mark is confined below 2 km and along which strong wind convergence as well as a substantial virtual potential temperature gradient are simulated. Most parcels found in large updraughts near the simulated precipitation maximum are lifted above CF1. Regarding the quasi-stationary location of CF1, the ~~REF~~ simulation indicates that CF1 ~~reached a sort of equilibrium with the LLJ blowing in the opposite direction. This equilibrium broke when the wind speed dropped, which caused~~ propagation towards

east is countered by the LLJ that blows in the opposite direction: when the wind speed drops, the cold air mass west of CF1 ~~to flow rapidly eastwards~~ flows rapidly eastwards which breaks the stationarity. A sensitivity study shows that evaporative cooling plays no role in the stationarity of CF1~~. One reason may be~~ , possibly because of the low evaporation due to the near saturation of the middle and lower troposphere~~, to which Leslie's remnants contributed. The location where CF1 remained quasi-stationary appears correlated with the location of the maximum precipitation in both simulation and observation.~~ .

Consequently, in decreasing order of importance, the location of the exceptional precipitation over the Aude department ~~seems the result of the convective activity~~ is the result of convection focusing (i) west of the quasi-stationary CF1 and (ii) downwind of the Albera Massif and the Corbières Massif. Precipitation maximum is found at the junction between these areas in both simulation and observation. Regarding the role of Leslie's remnants, they ~~(i) are involved in the formation of the cold front CF2 behind which a Mediterranean low deepened rapidly, (ii) contributed to the supply of~~ contribute to (i) supply low-level conditionally unstable air in the second part of the event and (~~iii) contributed to~~ ii) moisten mid-levels of the troposphere, diminishing evaporation processes which therefore play no role in modifying the location of CF1. However, low-level moisture that ~~contributed~~ contributes to precipitation over the Aude department mainly ~~originated from the Mediterranean Sea, east of 4.5 E,~~ originates from air masses located east of the Balearic Islands rather than Leslie's remnants.

Future work could quantify Leslie's ~~contribution in the cyclogenesis mechanisms of this Mediterranean low and more generally the role of ex-tropical cyclones in disturbing weather of the Mediterranean basin. Accurately track and represent the life cycle of Mediterranean lows seems crucial to better forecast HPEs. The use of near-surface analyses built from a large number of standard and personal weather stations , independent of the model studied, was beneficial in this case, helping to understand the inevitable departures between simulation and observation. It also highlighted small-scale movements of the quasi-stationary front CF1 that are simulated by the model but cannot be seized by the surface network. Future work could focus on real time tracking of~~ direct contribution in the formation of the Mediterranean low and its associated cold front CF2 but also the remote impact of Leslie's extratropical transition in a similar way as Grams and Blumer (2015) or Pantillon et al. (2015) : it could help to understand how accurately these systems need to be tracked to improve HPE forecasts. As they allow to track low-level ~~mesoscale boundaries which are involved in the~~ mesoscale boundaries which are involved in the stationarity of ~~precipitation. In order to do that, rapidly updated~~ precipitation, rapidly updated near-surface ~~thermodynamical analyses, only derived from observations and independent of models, seems promising. They could allow forecasters to evaluate in real time the~~ analyses comprising personal weather stations could be used as an independent means to evaluate in real time the accuracy of ~~near-surface fields forecasted by numerical models. In parallel, the assimilation of personal weather stations, supplementary observations that contributed to the quality of the near-surface analyses used in this study, could be tested in~~ near-surface model forecasts. In parallel, the assimilation of these station data could be tested in convective-scale ~~models like AROME~~models such as AROME.

## Appendix A: Details on the Meso-NH configuration

The lateral coupling is performed through a combination of a radiation boundary condition and a five-grid-point flow relaxation scheme with a damping rate of 0.002 $s^{-1}$. Near the upper boundary, a Rayleigh damping with a rate of 0.001 $s^{-1}$ is progressively applied above 15 km height in order to prevent spurious reflections. Both dampings are applied to the perturbations of the wind components and the thermodynamical variables with respect to their large-scale values.

The transport scheme chosen is a fourth-order centred discretization for the momentum and a monotonic version of the Piecewise Parabolic Method (Colella and Woodward, 1984) for meteorological (temperature, water substances and turbulent kinetic energy) and scalar variables. The time integration scheme is a fourth-order explicit Runge-Kutta for the momentum and a forward scheme for meteorological and scalar variables. The model time step is 2 s for the parent domain, 1 s for the child domain. To suppress very short wavelength modes, a fourth-order diffusion operator is applied to the wind components (u,v,w) with an e-folding time (time at which waves are damped by a factor $e^{-1}$) of 1800 s.

Earth surface variables and fluxes are simulated with the SURFEX model version 8.1 (Masson et al., 2013). Each grid mesh is divided in four main tiles. The following schemes are used for each tile: a three layer force-restore version of ISBA for natural land surface (Noilhan and Planton, 1989), TEB for urban area (Masson, 2000), the roughness length formula of Charnock (1955) with Louis (1979) exchange coefficients for lake and the COARE 3.0 parameterization (Fairall et al., 2003) for sea-surface fluxes. Optional corrections of sea-surface fluxes due to density effects during heat and water vapour transfer (Webb et al., 1980) and precipitation effects (Gosnell et al., 1995; Fairall et al., 1996) are applied. The SST field comes from the initial AROME analysis and remains constant for the entire simulation. Physiographic files used include the land cover data base ECOCLIMAP-II/Europe version 2.5 (Faroux et al., 2013), SRTM topography (Farr et al., 2007) and soil properties derived from the Harmonized World Soil Database (FAO, IIASA, ISRIC, ISS-CAS, JRC, 2012).

Regarding physical parameterizations, the longwave radiation scheme used is the Rapid Radiation Transfer Model (Mlawer et al., 1997) while the shortwave scheme is based on Fouquart and Bonnel (1980) method. For turbulence, the one dimensional parameterization used is based on a 1.5-order closure (Cuxart et al., 2000) of the turbulent kinetic energy equation with the Bougeault and Lacarrere (1989) mixing length. For the child model at 500 m horizontal resolution, in the so-called turbulence "grey zone", the choice of a 1D turbulence parameterization can be questioned (Machado and Chaboureau, 2015). Here, this choice is made to keep consistency between the two coupled models. At resolutions lower or equal to 1 km, deep convection is assumed to be resolved explicitly by the model's dynamics. Shallow convection is parameterized with the Pergaud et al. (2009) scheme. The bulk one-moment mixed microphysical scheme used is ICE3 (Pinty and Jabouille, 1998) that includes six water species (water vapour, cloud droplets, raindrops, pristine ice crystals, snow or aggregates and graupel).

*Code availability.* The Meso-NH model is freely available online at http://mesonh.aero.obs-mip.fr/mesonh54.

*Data availability.* Standard weather stations data, manual rain gauges data, radar mosaic, SPWS ANTILOPE QPE, ARPEGE and AROME analyses are provided by and property of Météo-France. World Meteorological Organization essential weather stations data, radar mosaic

at a 15 min time step, ARPEGE and AROME models are available in real time at https://donneespubliques.meteofrance.fr/. Direct online access of most datasets used in the study is not available: most of them can be provided on demand by the corresponding author only for research purposes.

*Author contributions.* This work was carried out by MM as part of his PhD thesis under the supervision of OC. MM and OC designed the study, interpreted the results and wrote the paper.

*Competing interests.* The authors declare that they have no conflict of interest.

*Acknowledgements.* This work is a contribution to the HyMeX programme supported by MISTRALS. We wish to particularly thank Quentin Rodier as well as the PHY-NH and PRECIP teams for valuable discussions about the Meso-NH model.

## References


Ayphassorho, H., Pipien, G., Guion de Meritens, I., and Lacroix, D.: Retour d'expérience des inondations du 14 au 17 octobre 2018 dans l'Aude, https://cgedd.documentation.developpement-durable.gouv.fr/notice?id=Affaires-0011552&reqId=548839ae-f685-4c3d-bbdb-9452154f508c&pos=12 (last access: 15 October 2020), 2019.

Barrett, A. I., Gray, S. L., Kirshbaum, D. J., Roberts, N. M., Schultz, D. M., and Fairman Jr, J. G.: Synoptic versus orographic control on stationary convective banding, Quarterly Journal of the Royal Meteorological Society, 141, 1101–1113, https://doi.org/10.1002/qj.2409, 2015.

Bougeault, P. and Lacarrere, P.: Parameterization of Orography-Induced Turbulence in a Mesobeta–Scale Model, Monthly Weather Review, 117, 1872–1890, https://doi.org/10.1175/1520-0493(1989)117<1872:POOITI>2.0.CO;2, 1989.

Bouin, M.-N., Redelsperger, J.-L., and Lebeaupin Brossier, C.: Processes leading to deep convection and sensitivity to sea-state representation during HyMeX IOP8 heavy precipitation event, Quarterly Journal of the Royal Meteorological Society, 143, 2600–2615, https://doi.org/10.1002/qj.3111, 2017.

Bresson, E., Ducrocq, V., Nuissier, O., Ricard, D., and de Saint-Aubin, C.: Idealized numerical simulations of quasi-stationary convective systems over the Northwestern Mediterranean complex terrain, Quarterly Journal of the Royal Meteorological Society, 138, 1751–1763, https://doi.org/10.1002/qj.1911, 2012.

Brousseau, P., Seity, Y., Ricard, D., and Léger, J.: Improvement of the forecast of convective activity from the AROME-France system, Quarterly Journal of the Royal Meteorological Society, 142, 2231–2243, https://doi.org/10.1002/qj.2822, 2016.

Caniaux, G., Redelsperger, J.-L., and Lafore, J.-P.: A Numerical Study of the Stratiform Region of a Fast-Moving Squall Line. Part I: General Description and Water and Heat Budgets, Journal of the Atmospheric Sciences, 51, 2046–2074, https://doi.org/10.1175/1520-0469(1994)051<2046:ANSOTS>2.0.CO;2, 1994.

Caumont, O., Mandement, M., Bouttier, F., Eeckman, J., Lebeaupin Brossier, C., Lovat, A., Nuissier, O., and Laurantin, O.: The heavy precipitation event of 14–15 October 2018 in the Aude catchment: A meteorological study based on operational numerical weather prediction systems and standard and personal observations, Natural Hazards and Earth System Sciences Discussions, 2020, 1–38, https://doi.org/10.5194/nhess-2020-310, 2020.

Caumont, O., Mandement, M., Bouttier, F., Eeckman, J., Lebeaupin Brossier, C., Lovat, A., Nuissier, O., and Laurantin, O.: The heavy precipitation event of 14–15 October 2018 in the Aude catchment: a meteorological study based on operational numerical weather prediction systems and standard and personal observations, Natural Hazards and Earth System Sciences, 21, 1135–1157, https://doi.org/10.5194/nhess-21-1135-2021, https://nhess.copernicus.org/articles/21/1135/2021/, 2021.

Champeaux, J.-L., Dupuy, P., Laurantin, O., Soulan, I., Tabary, P., and Soubeyroux, J.-M.: Les mesures de précipitations et l'estimation des lames d'eau à Météo-France : état de l'art et perspectives, La Houille Blanche, pp. 28–34, https://doi.org/10.1051/lhb/2009052, 2009.

Chappell, C. F.: Quasi-Stationary Convective Events, pp. 289–310, American Meteorological Society, Boston, MA, https://doi.org/10.1007/978-1-935704-20-1_13, 1986.

Charnock, H.: Wind stress on a water surface, Quarterly Journal of the Royal Meteorological Society, 81, 639–640, https://doi.org/10.1002/qj.49708135027, 1955.

Chazette, P., Flamant, C., Shang, X., Totems, J., Raut, J.-C., Doerenbecher, A., Ducrocq, V., Fourrié, N., Bock, O., and Cloché, S.: A multi-instrument and multi-model assessment of atmospheric moisture variability over the western Mediterranean during HyMeX, Quarterly Journal of the Royal Meteorological Society, 142, 7–22, https://doi.org/10.1002/qj.2671, 2016.

Chen, S.-H. and Lin, Y.-L.: Effects of Moist Froude Number and CAPE on a Conditionally Unstable Flow over a Mesoscale Mountain Ridge, Journal of the Atmospheric Sciences, 62, 331–350, https://doi.org/10.1175/JAS-3380.1, 2005.

Colella, P. and Woodward, P. R.: The Piecewise Parabolic Method (PPM) for gas-dynamical simulations, Journal of Computational Physics, 54, 174–201, https://doi.org/10.1016/0021-9991(84)90143-8, 1984.

Cosma, S., Richard, E., and Miniscloux, F.: The role of small-scale orographic features in the spatial distribution of precipitation, Quarterly Journal of the Royal Meteorological Society, 128, 75–92, https://doi.org/10.1256/00359000260498798, 2002.

Courtier, P., Freydier, C., Geleyn, J.-F., Rabier, F., and Rochas, M.: The Arpege project at Météo-France, in: Seminar on Numerical Methods in Atmospheric Models, 9–13 September 1991, vol. 2, pp. 193–232, ECMWF, https://www.ecmwf.int/node/8798, 1991.

Cuxart, J., Bougeault, P., and Redelsperger, J.-L.: A turbulence scheme allowing for mesoscale and large-eddy simulations, Quarterly Journal of the Royal Meteorological Society, 126, 1–30, https://doi.org/10.1002/qj.49712656202, 2000.

Davolio, S., Volonté, A., Manzato, A., Pucillo, A., Cicogna, A., and Ferrario, M. E.: Mechanisms producing different precipitation patterns over north-eastern Italy: insights from HyMeX-SOP1 and previous events, Quarterly Journal of the Royal Meteorological Society, 142, 188–205, https://doi.org/10.1002/qj.2731, 2016.

Davolio, S., Fera, S. D., Laviola, S., Miglietta, M. M., and Levizzani, V.: Heavy Precipitation over Italy from the Mediterranean Storm "Vaia" in October 2018: Assessing the Role of an Atmospheric River, Monthly Weather Review, 148, 3571 – 3588, https://doi.org/10.1175/MWR-D-20-0021.1, https://journals.ametsoc.org/view/journals/mwre/148/9/mwrD200021.xml, 2020.

Di Girolamo, P., Flamant, C., Cacciani, M., Richard, E., Ducrocq, V., Summa, D., Stelitano, D., Fourrié, N., and Saïd, F.: Observation of low-level wind reversals in the Gulf of Lion area and their impact on the water vapour variability, Quarterly Journal of the Royal Meteorological Society, 142, 153–172, https://doi.org/10.1002/qj.2767, 2016.

Drobinski, P., Ducrocq, V., Alpert, P., Anagnostou, E., Béranger, K., Borga, M., Braud, I., Chanzy, A., Davolio, S., Delrieu, G., Estournel, C., Boubrahmi, N. F., Font, J., Grubišić, V., Gualdi, S., Homar, V., Ivančan-Picek, B., Kottmeier, C., Kotroni, V., Lagouvardos, K., Lionello, P., Llasat, M. C., Ludwig, W., Lutoff, C., Mariotti, A., Richard, E., Romero, R., Rotunno, R., Roussot, O., Ruin, I., Somot, S., Taupier-Letage, I., Tintore, J., Uijlenhoet, R., and Wernli, H.: HyMeX: A 10-Year Multidisciplinary Program on the Mediterranean Water Cycle, Bulletin of the American Meteorological Society, 95, 1063–1082, https://doi.org/10.1175/BAMS-D-12-00242.1, 2014.

Ducrocq, V., Nuissier, O., Ricard, D., Lebeaupin, C., and Thouvenin, T.: A numerical study of three catastrophic precipitating events over southern France. II: Mesoscale triggering and stationarity factors, Quarterly Journal of the Royal Meteorological Society, 134, 131–145, https://doi.org/10.1002/qj.199, 2008.

Ducrocq, V., Braud, I., Davolio, S., Ferretti, R., Flamant, C., Jansa, A., Kalthoff, N., Richard, E., Taupier-Letage, I., Ayral, P.-A., Belamari, S., Berne, A., Borga, M., Boudevillain, B., Bock, O., Boichard, J.-L., Bouin, M.-N., Bousquet, O., Bouvier, C., Chiggiato, J., Cimini, D., Corsmeier, U., Coppola, L., Cocquerez, P., Defer, E., Delanoë, J., Di Girolamo, P., Doerenbecher, A., Drobinski, P., Dufournet, Y., Fourrié, N., Gourley, J. J., Labatut, L., Lambert, D., Le Coz, J., Marzano, F. S., Molinié, G., Montani, A., Nord, G., Nuret, M., Ramage, K., Rison, W., Roussot, O., Said, F., Schwarzenboeck, A., Testor, P., Van Baelen, J., Vincendon, B., Aran, M., and Tamayo, J.: HyMeX-SOP1: The Field Campaign Dedicated to Heavy Precipitation and Flash Flooding in the Northwestern Mediterranean, Bulletin of the American Meteorological Society, 95, 1083–1100, https://doi.org/10.1175/BAMS-D-12-00244.1, 2014.

Ducrocq, V., Davolio, S., Ferretti, R., Flamant, C., Santaner, V. H., Kalthoff, N., Richard, E., and Wernli, H.: Introduction to the HyMeX Special Issue on 'Advances in understanding and forecasting of heavy precipitation in the Mediterranean through the HyMeX SOP1 field campaign', Quarterly Journal of the Royal Meteorological Society, 142, 1–6, https://doi.org/10.1002/qj.2856, 2016.

Duffourg, F. and Ducrocq, V.: Assessment of the water supply to Mediterranean heavy precipitation: a method based on finely designed water budgets, Atmospheric Science Letters, 14, 133–138, https://doi.org/10.1002/asl2.429, 2013.

Duffourg, F., Nuissier, O., Ducrocq, V., Flamant, C., Chazette, P., Delanoë, J., Doerenbecher, A., Fourrié, N., Di Girolamo, P., Lac, C., Legain, D., Martinet, M., Saïd, F., and Bock, O.: Offshore deep convection initiation and maintenance during the HyMeX IOP 16a heavy precipitation event, Quarterly Journal of the Royal Meteorological Society, 142, 259–274, https://doi.org/10.1002/qj.2725, 2016.

Duffourg, F., Lee, K.-O., Ducrocq, V., Flamant, C., Chazette, P., and Di Girolamo, P.: Role of moisture patterns in the backbuilding formation of HyMeX IOP13 heavy precipitation systems, Quarterly Journal of the Royal Meteorological Society, 144, 291–303, https://doi.org/10.1002/qj.3201, 2018.

Fairall, C. W., Bradley, E. F., Rogers, D. P., Edson, J. B., and Young, G. S.: Bulk parameterization of air-sea fluxes for Tropical Ocean-Global Atmosphere Coupled-Ocean Atmosphere Response Experiment, Journal of Geophysical Research: Oceans, 101, 3747–3764, https://doi.org/10.1029/95JC03205, 1996.

Fairall, C. W., Bradley, E. F., Hare, J. E., Grachev, A. A., and Edson, J. B.: Bulk Parameterization of Air–Sea Fluxes: Updates and Verification for the COARE Algorithm, Journal of Climate, 16, 571–591, https://doi.org/10.1175/1520-0442(2003)016<0571:BPOASF>2.0.CO;2, 2003.

FAO, IIASA, ISRIC, ISS-CAS, JRC: Harmonized World Soil Database version 1.2, https://webarchive.iiasa.ac.at/Research/LUC/External-World-soil-database/HTML/ (last access: 15 October 2020), 2012.

Faroux, S., Kaptué Tchuenté, A. T., Roujean, J.-L., Masson, V., Martin, E., and Le Moigne, P.: ECOCLIMAP-II/Europe: a twofold database of ecosystems and surface parameters at 1 km resolution based on satellite information for use in land surface, meteorological and climate models, Geoscientific Model Development, 6, 563–582, https://doi.org/10.5194/gmd-6-563-2013, 2013.

Farr, T. G., Rosen, P. A., Caro, E., Crippen, R., Duren, R., Hensley, S., Kobrick, M., Paller, M., Rodriguez, E., Roth, L., Seal, D., Shaffer, S., Shimada, J., Umland, J., Werner, M., Oskin, M., Burbank, D., and Alsdorf, D.: The Shuttle Radar Topography Mission, Reviews of Geophysics, 45, RG2004, https://doi.org/10.1029/2005RG000183, 2007.

Fouquart, Y. and Bonnel, B.: Computations of solar heating of the Earth's atmosphere: a new parameterization, Beiträge zur Physik der Atmosphäre, 53, 35–62, 1980.

French Insurance Federation: The lethal floods that affected south-east France from 22-24 November caused losses with a provisional estimated cost of 285 million Euros, https://www.ffa-assurance.fr/en/media-room/press-release/lethal-floods-affected-south-east-france-22-24-november-caused-losses (last access: 15 October 2020), 2019.

Gal-Chen, T. and Somerville, R. C.: On the use of a coordinate transformation for the solution of the Navier-Stokes equations, Journal of Computational Physics, 17, 209 – 228, https://doi.org/10.1016/0021-9991(75)90037-6, 1975.

Gheusi, F. and Stein, J.: Lagrangian description of airflows using Eulerian passive tracers, Quarterly Journal of the Royal Meteorological Society, 128, 337–360, https://doi.org/10.1256/00359000260498914, 2002.

Gosnell, R., Fairall, C. W., and Webster, P. J.: The sensible heat of rainfall in the tropical ocean, Journal of Geophysical Research: Oceans, 100, 18 437–18 442, https://doi.org/10.1029/95JC01833, 1995.

Grams, C. M. and Blumer, S. R.: European high-impact weather caused by the downstream response to the extratropical transition of North Atlantic Hurricane Katia (2011), Geophysical Research Letters, 42, 8738–8748, https://doi.org/10.1002/2015GL066253, 2015.

Kirshbaum, D. J., Adler, B., Kalthoff, N., Barthlott, C., and Serafin, S.: Moist Orographic Convection: Physical Mechanisms and Links to Surface-Exchange Processes, Atmosphere, 9, https://doi.org/10.3390/atmos9030080, 2018.

Kreitz, M., Calas, C., and Baille, S.: Inondations de l'Aude du 15 octobre 2018 : analyse météorologique, conséquences hydrologiques et prévisibilité, La Météorologie, 8$^{e}$ série, n°110, pp. 46–64, https://doi.org/10.37053/lameteorologie-2020-0067, 2020.

Lac, C., Chaboureau, J.-P., Masson, V., Pinty, J.-P., Tulet, P., Escobar, J., Leriche, M., Barthe, C., Aouizerats, B., Augros, C., Aumond, P., Auguste, F., Bechtold, P., Berthet, S., Bielli, S., Bosseur, F., Caumont, O., Cohard, J.-M., Colin, J., Couvreux, F., Cuxart, J., Delautier, G., Dauhut, T., Ducrocq, V., Filippi, J.-B., Gazen, D., Geoffroy, O., Gheusi, F., Honnert, R., Lafore, J.-P., Lebeaupin Brossier, C., Libois, Q., Lunet, T., Mari, C., Maric, T., Mascart, P., Mogé, M., Molinié, G., Nuissier, O., Pantillon, F., Peyrillé, P., Pergaud, J., Perraud, E., Pianezze, J., Redelsperger, J.-L., Ricard, D., Richard, E., Riette, S., Rodier, Q., Schoetter, R., Seyfried, L., Stein, J., Suhre, K., Taufour, M., Thouron, O., Turner, S., Verrelle, A., Vié, B., Visentin, F., Vionnet, V., and Wautelet, P.: Overview of the Meso-NH model version 5.4 and its applications, Geoscientific Model Development, 11, 1929–1969, https://doi.org/10.5194/gmd-11-1929-2018, 2018.

Lebeaupin, C., Ducrocq, V., and Giordani, H.: Sensitivity of torrential rain events to the sea surface temperature based on high-resolution numerical forecasts, Journal of Geophysical Research: Atmospheres, 111, https://doi.org/10.1029/2005JD006541, 2006.

Lebeaupin Brossier, C., Ducrocq, V., and Giordani, H.: Two-way one-dimensional high-resolution air–sea coupled modelling applied to Mediterranean heavy rain events, Quarterly Journal of the Royal Meteorological Society, 135, 187–204, https://doi.org/10.1002/qj.338, 2009.

Lee, K.-O., Flamant, C., Duffourg, F., Ducrocq, V., and Chaboureau, J.-P.: Impact of upstream moisture structure on a back-building convective precipitation system in south-eastern France during HyMeX IOP13, Atmospheric Chemistry and Physics, 18, 16 845–16 862, https://doi.org/10.5194/acp-18-16845-2018, 2018.

Lorenzo-Lacruz, J., Amengual, A., Garcia, C., Morán-Tejeda, E., Homar, V., Maimó-Far, A., Hermoso, A., Ramis, C., and Romero, R.: Hydro-meteorological reconstruction and geomorphological impact assessment of the October 2018 catastrophic flash flood at Sant Llorenç, Mallorca (Spain), Natural Hazards and Earth System Sciences, 19, 2597–2617, https://doi.org/10.5194/nhess-19-2597-2019, 2019.

Louis, J.-F.: A parametric model of vertical eddy fluxes in the atmosphere, Boundary-Layer Meteorology, 17, 187–202, https://doi.org/10.1007/BF00117978, 1979.

Machado, L. A. T. and Chaboureau, J.-P.: Effect of Turbulence Parameterization on Assessment of Cloud Organization, Monthly Weather Review, 143, 3246–3262, https://doi.org/10.1175/MWR-D-14-00393.1, 2015.

Mandement, M. and Caumont, O.: Contribution of personal weather stations to the observation of deep-convection features near the ground, Natural Hazards and Earth System Sciences, 20, 299–322, https://doi.org/10.5194/nhess-20-299-2020, 2020.

Martinet, M., Nuissier, O., Duffourg, F., Ducrocq, V., and Ricard, D.: Fine-scale numerical analysis of the sensitivity of the HyMeX IOP16a heavy precipitating event to the turbulent mixing-length parametrization, Quarterly Journal of the Royal Meteorological Society, 143, 3122–3135, https://doi.org/10.1002/qj.3167, 2017.

Masson, V.: A Physically-Based Scheme For The Urban Energy Budget In Atmospheric Models, Boundary-Layer Meteorology, 94, 357–397, https://doi.org/10.1023/A:1002463829265, 2000.

Masson, V., Le Moigne, P., Martin, E., Faroux, S., Alias, A., Alkama, R., Belamari, S., Barbu, A., Boone, A., Bouyssel, F., Brousseau, P., Brun, E., Calvet, J.-C., Carrer, D., Decharme, B., Delire, C., Donier, S., Essaouini, K., Gibelin, A.-L., Giordani, H., Habets, F., Jidane, M., Kerdraon, G., Kourzeneva, E., Lafaysse, M., Lafont, S., Lebeaupin Brossier, C., Lemonsu, A., Mahfouf, J.-F., Marguinaud, P., Mokhtari, M., Morin, S., Pigeon, G., Salgado, R., Seity, Y., Taillefer, F., Tanguy, G., Tulet, P., Vincendon, B., Vionnet, V., and Voldoire, A.: The SURFEXv7.2 land and ocean surface platform for coupled or offline simulation of earth surface variables and fluxes, Geoscientific Model Development, 6, 929–960, https://doi.org/10.5194/gmd-6-929-2013, 2013.

Miglietta, M. M. and Rotunno, R.: Numerical Simulations of Sheared Conditionally Unstable Flows over a Mountain Ridge, Journal of the Atmospheric Sciences, 71, 1747–1762, https://doi.org/10.1175/JAS-D-13-0297.1, 2014.

Miltenberger, A. K., Pfahl, S., and Wernli, H.: An online trajectory module (version 1.0) for the nonhydrostatic numerical weather prediction model COSMO, Geoscientific Model Development, 6, 1989–2004, https://doi.org/10.5194/gmd-6-1989-2013, https://gmd.copernicus.org/articles/6/1989/2013/, 2013.

Miniscloux, F., Creutin, J. D., and Anquetin, S.: Geostatistical Analysis of Orographic Rainbands, Journal of Applied Meteorology, 40, 1835–1854, https://doi.org/10.1175/1520-0450(2001)040<1835:GAOOR>2.0.CO;2, 2001.

Mlawer, E. J., Taubman, S. J., Brown, P. D., Iacono, M. J., and Clough, S. A.: Radiative transfer for inhomogeneous atmospheres: RRTM, a validated correlated-k model for the longwave, Journal of Geophysical Research: Atmospheres, 102, 16 663–16 682, https://doi.org/10.1029/97JD00237, 1997.

NOAA NESDIS: Remnants of Hurricanes Michael and Leslie Reach Europe, https://www.nesdis.noaa.gov/content/remnants-hurricanes-michael-and-leslie-reach-europe (last access: 15 October 2020), 2018.

NOAA NWS National Hurricane Center: Hurricane Leslie Advisory Number 69, https://www.nhc.noaa.gov/archive/2018/al13/al132018.public.069.shtml (last access: 15 October 2020), 2018a.

NOAA NWS National Hurricane Center: Hurricane Leslie Advisory Number 70, https://www.nhc.noaa.gov/archive/2018/al13/al132018.public.070.shtml (last access: 15 October 2020), 2018b.

Noilhan, J. and Planton, S.: A Simple Parameterization of Land Surface Processes for Meteorological Models, Monthly Weather Review, 117, 536–549, https://doi.org/10.1175/1520-0493(1989)117<0536:ASPOLS>2.0.CO;2, 1989.

Nuissier, O., Ducrocq, V., Ricard, D., Lebeaupin, C., and Anquetin, S.: A numerical study of three catastrophic precipitating events over southern France. I: Numerical framework and synoptic ingredients, Quarterly Journal of the Royal Meteorological Society, 134, 111–130, https://doi.org/10.1002/qj.200, 2008.

Nuissier, O., Marsigli, C., Vincendon, B., Hally, A., Bouttier, F., Montani, A., and Paccagnella, T.: Evaluation of two convection-permitting ensemble systems in the HyMeX Special Observation Period (SOP1) framework, Quarterly Journal of the Royal Meteorological Society, 142, 404–418, https://doi.org/10.1002/qj.2859, 2016.

Pantillon, F., Chaboureau, J.-P., and Richard, E.: Remote impact of North Atlantic hurricanes on the Mediterranean during episodes of intense rainfall in autumn 2012, Quarterly Journal of the Royal Meteorological Society, 141, 967–978, https://doi.org/10.1002/qj.2419, https://rmets.onlinelibrary.wiley.com/doi/abs/10.1002/qj.2419, 2015.

Pergaud, J., Masson, V., Malardel, S., and Couvreux, F.: A Parameterization of Dry Thermals and Shallow Cumuli for Mesoscale Numerical Weather Prediction, Boundary-Layer Meteorology, 132, 1573–1472, https://doi.org/10.1007/s10546-009-9388-0, 2009.

Petrucci, O., Aceto, L., Bianchi, C., Bigot, V., Brázdil, R., Pereira, S., Inbar, M., Kahraman, A., Kılıç, O., Kotroni, V., Llasat, M. C., Llasat-Botija, M., Mercuri, M., Papagiannaki, K., Řehoř, J., Rossello-Geli, J., Salvati, P., Vinet, F., and Zêzere, J. L.: EUropean Flood Fatalities (EUFF) database 1980-2018 (updated), https://doi.org/10.4121/UUID:489D8A13-1075-4D2F-ACCB-DB7790E4542F, 2020.

Pinty, J.-P. and Jabouille, P.: A mixed-phase cloud parameterization for use in mesoscale non-hydrostatic model: simulations of a squall line and of orographic precipitations., in: Proceedings of the Conference of Cloud Physics 17–21 August 1998, Everett, WA, USA, American Meteorological Society, pp. 217–220, 1998.

Préfecture de l'Aude: Communiqué de presse du 17 octobre 2018, http://www.aude.gouv.fr/IMG/pdf/20181017_cp_21h00.pdf (last access: 15 October 2020), 2018.

Rainaud, R., Lebeaupin Brossier, C., Ducrocq, V., Giordani, H., Nuret, M., Fourrié, N., Bouin, M.-N., Taupier-Letage, I., and Legain, D.: Characterization of air–sea exchanges over the Western Mediterranean Sea during HyMeX SOP1 using the AROME–WMED model, Quarterly Journal of the Royal Meteorological Society, 142, 173–187, https://doi.org/10.1002/qj.2480, 2016.

Reinecke, P. A. and Durran, D. R.: Estimating Topographic Blocking Using a Froude Number When the Static Stability Is Nonuniform, Journal of the Atmospheric Sciences, 65, 1035–1048, https://doi.org/10.1175/2007JAS2100.1, 2008.

Ricard, D.: Modélisation à haute résolution : des pluies intenses dans les Cévennes – Le système convectif des 13 et 14 octobre 1995, La Météorologie, 8$^{e}$ série, n°7, pp. 28–38, https://doi.org/10.4267/2042/56316, 2005.

Ricard, D., Ducrocq, V., and Auger, L.: A Climatology of the Mesoscale Environment Associated with Heavily Precipitating Events over a Northwestern Mediterranean Area, Journal of Applied Meteorology and Climatology, 51, 468–488, https://doi.org/10.1175/JAMC-D-11-017.1, 2012.

Santurette, P. and Joly, A.: ANASYG/PRESYG, Météo-France's new graphical summary of the synoptic situation, Meteorological Applications, 9, 129–154, https://doi.org/10.1017/S1350482702002013, 2002.

Schär, C. and Wernli, H.: Structure and evolution of an isolated semi-geostrophic cyclone, Quarterly Journal of the Royal Meteorological Society, 119, 57–90, https://doi.org/10.1002/qj.49711950904, https://rmets.onlinelibrary.wiley.com/doi/abs/10.1002/qj.49711950904, 1993.

Seity, Y., Brousseau, P., Malardel, S., Hello, G., Bénard, P., Bouttier, F., Lac, C., and Masson, V.: The AROME-France Convective-Scale Operational Model, Monthly Weather Review, 139, 976–991, https://doi.org/10.1175/2010MWR3425.1, 2011.

Trapero, L., Bech, J., and Lorente, J.: Numerical modelling of heavy precipitation events over Eastern Pyrenees: Analysis of orographic effects, Atmospheric Research, 123, 368–383, https://doi.org/10.1016/j.atmosres.2012.09.014, 6th European Conference on Severe Storms 2011. Palma de Mallorca, Spain, 2013.

Webb, E. K., Pearman, G. I., and Leuning, R.: Correction of flux measurements for density effects due to heat and water vapour transfer, Quarterly Journal of the Royal Meteorological Society, 106, 85–100, https://doi.org/10.1002/qj.49710644707, 1980.